Earth Syst. Sci. Data, 18, 5069–5092, 2026
https://doi.org/10.5194/essd-18-5069-2026

Open Access Earth System Science Data

Jingwei-Nutrients: a global spatiotemporal reconstruction of ocean nutrients (1965–2023) using multi-task deep learning

Zhaokun Wang[1], Bin Lu[1], Yi Xin[1], Takamitsu Ito[2], Lei Zhou[3], Lijing Cheng[4], Yuanlong Li[5], Xinbing Wang[1], and Meng Jin[6]

[1]School of Information Science and Electronic Engineering, Shanghai Jiao Tong University, Shanghai 200240, China
[2]School of Earth and Atmospheric Sciences, Georgia Institute of Technology, Atlanta, GA 30332, USA
[3]School of Oceanography, Shanghai Jiao Tong University, Shanghai 200030, China
[4]State Key Laboratory of Earth System Numerical Modeling and Application, Institute of Atmospheric Physics, Chinese Academy of Sciences, Beijing 100029, China
[5]Key Laboratory of Ocean Observation and Forecasting and Key Laboratory of Ocean Circulation and Waves, Institute of Oceanology, Chinese Academy of Sciences, Qingdao 266071, China
[6]School of Artificial Intelligence, Shanghai Jiao Tong University, Shanghai 200240, China

Correspondence: Bin Lu (robinlu1209@sjtu.edu.cn) and Meng Jin (jinm@sjtu.edu.cn)

Received: 23 April 2026 – Discussion started: 12 May 2026
Revised: 3 July 2026 – Accepted: 13 July 2026 – Published: 20 July 2026

Abstract. Dissolved nitrate, phosphate, and silicate are fundamental drivers of marine primary productivity and the biological carbon pump. However, the development of continuous, long-term global datasets has long been severely hindered by extreme historical data sparsity and complex biogeochemical dynamics. Statistical interpolation methods struggle to simultaneously fill the severely sparse data gaps and capture the non-linear interactions, necessitating advanced artificial intelligence (AI) to explicitly learn and leverage their underlying relationships. Nevertheless, most existing AI methods reconstruct nutrients independently (i.e., Single-Task Learning), failing to exploit the synergistic effects inherent in cross-nutrient stoichiometry. In this study, we present *Jingwei-Nutrients*, a four-dimensional global monthly data product at $1^\circ \times 1^\circ$ resolution from 0 to 2000 m depth spanning 1965 to 2023, reconstructed using a Transformer-based Multi-Task Learning (MTL) framework trained on a comprehensive, quality-controlled multi-source observational database. Evaluation on chronological K-fold cross-validation yields mean validation R^2 values across folds of 0.991, 0.969, and 0.990, with RMSEs of 1.295, 0.163, and 4.109 $\mu mol\,kg^{-1}$ for nitrate, phosphate, and silicate, respectively. Temporal K-fold cross-validation reveals that the MTL framework consistently achieves higher R^2 and lower RMSE for all three nutrients compared to single-task models, with larger accuracy gains in data-sparse earlier decades such as 1965–1975. Our data product reproduces consistent global climatology patterns and seasonal cycles with World Ocean Atlas (WOA). Furthermore, independent evaluations against long-term monitoring stations (HOT and KERFIX) and GO-SHIP cruise sections (P16N, P16S, and P06E) demonstrate our effectiveness across multi-decadal temporal trends, spatial variability and vertical changes. Additionally, an ensemble-based uncertainty analysis reveals interpretable spatial heterogeneities and a long-term decreasing trend in global uncertainty, which directly mirrors the historical transition from sparse early sampling to modern observing networks. This product fills a critical gap in historical ocean biogeochemical observations, providing a reliable, physically consistent foundation for marine biogeochemical modeling and climate change studies. The product is openly available at https://doi.org/10.5281/zenodo.21066027 (Wang et al., 2026).

1 Introduction

Nutrients – specifically nitrate, phosphate, and silicate – serve as the fundamental basis for marine ecosystems and function as critical drivers of ocean biogeochemistry (Sigman and Hain, 2012; Moore et al., 2013). Nitrate is often the proximate limiting nutrient in much of the low-latitude surface ocean, directly constraining phytoplankton growth and ecosystem productivity (Moore et al., 2013; Browning and Moore, 2023). Phosphate, while also a limiting factor in specific regions, plays a distinct role in regulating long-term ocean fertility and metabolic processes over geological timescales (Deutsch and Weber, 2012). Silicate is essential for diatoms – a key phytoplankton group responsible for a large fraction of carbon export – thereby controlling the efficiency of the biological pump and the sequestration of atmospheric CO_2 (Benitez-Nelson et al., 2007; Tréguer et al., 2018). Collectively, the availability and concentrations of these dissolved inorganic nutrients determine the magnitude of primary and new production across the global ocean (Fasham, 2003; Moore et al., 2013).

Although these nutrients serve distinct ecological and biogeochemical roles, they do not operate in isolation. Because these nutrients collectively fuel the biological pump, their distributions in the marine environment do not vary independently; rather, they are tightly coupled through biological uptake and regeneration processes (Deutsch and Weber, 2012). Phytoplankton consume nitrate, phosphate, and silicate in fundamentally consistent average stoichiometric proportions during photosynthesis and release them back into the water column during remineralization, establishing a robust biogeochemical linkage among their cycles (Redfield, 1934). However, contemporary syntheses reveal that rather than being rigidly static, this marine ecological stoichiometry is highly dynamic, exhibiting pronounced shifts across large-scale spatial gradients and multi-decadal timescales (Liu et al., 2025). This intrinsic, yet variable, coupling implies that the spatial and temporal distribution of one element is dynamically constrained by the others (Sarmiento and Gruber, 2006). Furthermore, the interplay between these shifting biological drivers and physical transport processes, such as water mass mixing, results in complex, non-linear hydrographic relationships that vary dynamically with depth and latitude (Ascani et al., 2013).

Despite their biogeochemical significance and the predictable nature of their elemental coupling, observational data for these nutrients remain limited. While physical variables such as temperature and salinity are now extensively monitored at high spatiotemporal resolution by autonomous platforms like the core Argo array (Roemmich et al., 2019), nutrient concentrations have historically been derived from discrete shipboard sampling and subsequent laboratory analysis (Olsen et al., 2016). Although the advent of the Biogeochemical-Argo (BGC-Argo) program has expanded autonomous nitrate monitoring (Claustre et al., 2020), comparable sensors for phosphate and silicate are not yet available. Consequently, the historical reliance on labor-intensive and costly ship-based operations has resulted in spatiotemporal discontinuities in the global nutrient database. Historical observations are heavily biased toward the Northern Hemisphere and summer months, leaving large regions of the Southern Ocean and the deep sea poorly sampled, particularly during winter seasons (Garcia et al., 2018). Ultimately, this scarcity of continuous, four-dimensional observations hinders our ability to fully resolve the multi-scale variability of global nutrient cycles and their ecosystem responses to climate change.

To bridge these observational gaps and generate global nutrient fields, the oceanographic community has developed various mapping strategies over the past decades. Traditional approaches predominantly employ objective analysis or optimal interpolation techniques to map discrete nutrient profiles onto regular spatial grids (e.g., Levitus, 1982; Garcia et al., 2018). However, these statistical interpolation methods require high-density spatial coverage to maintain accuracy. Given the sparsity of historical nutrient observations, these methods are typically limited in capturing the temporal dimension, often aggregating decades of discrete sampling data to construct a single, temporally averaged background field. This spatial-temporal trade-off has led to the development of highly valuable but static climatological products, most notably the World Ocean Atlas (WOA) (Garcia et al., 2018, 2024a). Consequently, while such gridded climatologies provide a crucial baseline for the oceanic mean state, they lose temporal variance and multi-decadal biogeochemical trends, rendering them insufficient for resolving continuous, long-term global nutrient variability.

To address these limitations of statistical interpolation, machine learning (ML) algorithms have emerged as alternative tools capable of resolving complex, non-linear biogeochemical dynamics even within data-sparse regimes (Sauzède et al., 2017; Bittig et al., 2018; Ito et al., 2024; Lu et al., 2024). By leveraging empirical relationships between target biogeochemical variables and widely available physical predictors (e.g., temperature and salinity), these data-driven models can infer missing concentrations and reconstruct continuous fields. Building upon this paradigm, neural networks and ensemble methods have been validated across various oceanographic domains. For instance, they have demonstrated reliability in mapping global ocean carbon parameters and dissolved oxygen inventories (Landschützer et al., 2016; Gregor et al., 2019; Ito et al., 2017), indicating the capability of ML to capture intricate hydrographic couplings. Encouraged by these successes, recent machine learning approaches have been extended to macronutrient reconstruction, yielding valuable specialized products that focus on surface fields, regional domains, or individual nutrient variables, such as satellite-derived global surface macronutrient estimates, pan-European nitrate reconstructions, and historical nutrient reconstructions for the North Pacific (Sundararaman and Shanmugam, 2024; Yu et al., 2025; Du et al., 2026).

Despite these promising ML applications, a limitation persists across nearly all existing nutrient reconstruction frameworks: they rely on Single-Task Learning (STL) paradigms. In these conventional models, nitrate, phosphate, and silicate are treated as independent targets, with a separate neural network trained for each element. This isolated training process does not account for the stoichiometric coupling that governs ocean biogeochemistry (e.g., Redfield, 1934; Deutsch and Weber, 2012). Consequently, single-task models cannot mutually constrain their multi-element predictions, which can lead to physically inconsistent elemental ratios within the reconstructed fields, particularly across vast, data-sparse oceanic domains. Furthermore, STL models impose rigid data requirements, demanding exact target availability for training. For instance, if a historical observation contains valid phosphate measurements but lacks nitrate, the entire profile is discarded during the training of the nitrate model. Consequently, the valuable hydrographic context embedded in that observation cannot be utilized to inform the coupled biogeochemical system. This fragmented approach leads to an underutilization of the already scarce historical data archives, further reducing the available training pool.

Recognizing the limitation of single-task models and the scarcity of continuous global time-series products, we design a Multi-Task Learning (MTL) framework (Kendall et al., 2018; Yu et al., 2020) based on the Transformer architecture (Vaswani et al., 2017). The idea of multi-task learning is to train a single model to tackle multiple related tasks at once, enabling progress in one task to implicitly benefit the others. This joint learning approach leverages the intrinsic biogeochemical stoichiometry among nitrate, phosphate, and silicate. By allowing data-rich targets to serve as auxiliary constraints for under-sampled variables, the MTL architecture maximizes the utility of fragmented historical observations, particularly in data-sparse eras. Employing this framework, we present *Jingwei-Nutrients*, a four-dimensional spatiotemporal data product of global ocean nutrients spanning from 1965 to 2023 (An explanation of the name *Jingwei* is provided in the section "The Name of Jingwei"). Driven by quality-controlled in situ nutrient archives and hydrographic physical predictors, the product provides continuous, monthly oceanic fields at a $1^\circ \times 1^\circ$ spatial resolution, covering the global ocean from the surface down to a depth of 2000 m.

To verify the physical and biological representation of the reconstructed fields, we conduct multi-scale validations. These assessments include time-based K-fold cross-validation and comparative evaluations against single-task models to assess the performance of the MTL framework. Additionally, we conduct global climatology comparisons to evaluate large-scale spatial patterns and seasonal cycles, alongside independent verifications against long-term ecological time-series stations (HOT and KERFIX), and cross-section evaluations using GO-SHIP cruise sections (P16N, P16S, and P06E). Furthermore, we incorporate an ensemble-based spatiotemporal uncertainty analysis to quantify model variance and track the historical evolution of reconstruction uncertainties. Ultimately, the Jingwei-Nutrients product offers a validated and biogeochemically coherent baseline for investigating multi-decadal ocean biogeochemical dynamics and ecosystem responses to global climate change.

To facilitate community access and dynamic data exploration, we develop a dedicated scientific web platform (https://jingwei.acemap.info, last access: 16 July 2026). Beyond standard data distribution and visualization, this interactive platform integrates advanced analytical tools, allowing researchers to perform on-the-fly scientific computing, such as generating real-time vertical cross-sections and analyzing long-term time-series trajectories, directly supporting regional or global biogeochemical studies.

2 Data and Methods

2.1 Observation Data

To construct the observational targets and training features for the global nutrient reconstruction, we compile a database of historical in situ observations spanning from 1965 to 2023. The target variables – specifically dissolved inorganic nitrate, phosphate, and silicate – are harmonized from quality-controlled public archives, primarily the World Ocean Database 2018 (WOD18; Boyer et al., 2018), the Global Ocean Data Analysis Project version 2 (GLODAPv2.2022; Lauvset et al., 2022), the CLIVAR and Carbon Hydrographic Data Office (CCHDO; Sloyan et al., 2019), and the Biogeochemical-Argo (BGC-Argo) program (Claustre et al., 2020). For BGC-Argo nitrate, we use the officially adjusted profiles with calibration information to reduce sensor-drift and calibration-related biases. The corresponding hydrographic predictors are sourced from the World Ocean Database 2023 (WOD23; Mishonov et al., 2024; Garcia et al., 2026) and collocated with these nutrient samples. Because our reconstruction model relies on the physical identification of water masses, we select only data containing concurrent temperature and salinity (T/S) measurements. To avoid data redundancy across these archives, duplicate profiles are identified and removed based on their spatiotemporal coordinates and cruise identifiers. Following data harmonization, deduplication, collocation, and quality control, the final dataset comprises 5 735 819 collocated T/S profiles. These physical features are paired with target nutrient observations, yielding a total of 4 225 374 nitrate, 3 578 340 phosphate, and 2 931 998 silicate measurements aggregated across the four archives. The detailed distribution of these observations per database is summarized in Table 1. The numbers in Table 1 represent the complete quality-controlled observational archive, while observations reserved for independent station and cruise-section validations are excluded from the training subset as described in Sect. 2.5.4.

2.2 Climatological Features

To provide the machine learning model with a consistent biogeochemical and physical mean state, we incorporate climatological fields from the World Ocean Atlas (WOA). We utilize a combination of the most recent available versions for different variables to ensure the highest data quality. These fields define the spatial reference grid for our study, featuring a $1^\circ \times 1^\circ$ horizontal resolution and 67 standard vertical levels (0–2000 m).

We select a total of six variables to characterize the background environment. Specifically, dissolved oxygen, oxygen saturation, and apparent oxygen utilization are obtained from the World Ocean Atlas 2023 (Garcia et al., 2024b). Climatologies for density and conductivity are sourced from the World Ocean Atlas 2018 (Locarnini et al., 2019; Reagan et al., 2019), while the mixed layer depth is derived from the WOA18 temperature and salinity fields (Locarnini et al., 2018; Zweng et al., 2018). These climatological inputs provide the mean state of the global ocean, serving as static "background" features for the machine learning model.

2.3 Time-Varying Hydrographic Predictors

For the global inference phase, we require continuous, time-varying, and historically consistent hydrographic inputs. We utilize the EN4.2.2 objective analysis dataset (Good et al., 2013), which provides monthly potential temperature and salinity fields from 1965 to 2023 at a $1^\circ \times 1^\circ$ resolution.

We select EN4 as the hydrographic predictors because of its systematic bias correction. EN4 integrates quality-controlled profiles from the World Ocean Database (WOD), the Global Telecommunication System (GTSPP), and the Argo array, while applying bias correction schemes (e.g., Gouretski and Reseghetti, 2010) to historical mechanical bathythermograph (MBT) and expendable bathythermograph (XBT) records. This processing reduces time-dependent instrumental biases, ensuring that the decadal trends in the input features represent physical variability rather than measurement artifacts.

Furthermore, the objective analysis framework of EN4 effectively bridges observational gaps, providing the spatiotemporally complete fields strictly required to drive global machine learning inferences. Because of its high fidelity in representing historical hydrographic environments, EN4 has been extensively validated as a foundational benchmark for capturing historical ocean heat storage and multi-decadal transport (Cheng et al., 2017; Zanna et al., 2019). Consequently, it is routinely employed as a highly reliable physical forcing dataset to drive large-scale data-driven biogeochemical mappings and carbon cycle reconstructions (Landschützer et al., 2016).

2.4 Data Quality Control

Because our dataset originates from diverse observational platforms and encompasses highly varied temporal and geographic scales, establishing a strict, multi-tiered quality control (QC) pipeline is critical to eliminate inaccurate records. Guided by the fundamental principles outlined in the World Ocean Database (WOD) documentation (Boyer et al., 2018), we implemented a three-stage hierarchical strategy on the merged global archive. This framework systematically filters hydrographic and nutrient variables at the measurement, station, and cruise levels.

The first level of our hierarchical QC protocol targets individual measurements, employing a sequence of seven specific checks to identify and remove potentially erroneous records from the combined datasets. (1) Initially, we apply a depth-specific boundary constraint optimized for our target 0–2000 m water column. By defining physically realistic domains for every variable across designated water strata, any observation exceeding these established boundaries is consequently rejected. This restriction covers temperature, salinity, and the three target nutrient parameters: nitrate (NO_3^-), phosphate (PO_4^{3-}), and silicate ($Si(OH)_4$). (2) We evaluate the biogeochemical consistency of the data by checking empirical relationships between paired variables. We validate observations against accepted theoretical spaces for both physical pairings (T–S) and physical-biogeochemical combinations (e.g., T–N, T–P, T–Si, S–N, S–P, S–Si) to guarantee alignment with recognized water mass signatures. (3) To capture extreme statistical anomalies, we compute the local mean and standard deviation for each standard depth horizon. Any value shifting beyond six standard deviations from its respective mean is tagged as an outlier. (4) We assess vertical continuity by calculating the vertical gradient for each parameter. Any measurement showing a vertical rate of change that exceeds the mean gradient by more than five standard deviations is marked as questionable. (5) A density inversion assessment targets physically improbable vertical structures. Since parameters such as temperature and nutrients typically exhibit monotonic relationships with depth or potential density (σ_θ) in stratified waters, measurements violating preset thresholds for relationships (e.g., Depth–T, Depth–Nutrient, or σ_θ–Nutrient) are flagged. (6) We identify vertical spikes by comparing each measurement directly against its immediate upper and lower neighbors. If this difference exceeds a preset limit, the observation is flagged as a spike. (7) Finally, we rely on the original quality flags provided by the source databases. We only retain measurements explicitly labeled as "good" and discard any records marked as questionable or bad.

Following the assessment of individual measurements, regarding to the second level, we extend the quality control

Table 1. Summary of nutrients and hydrographic data compiled from four major databases after quality control.

	WOD	CCHDO	GLODAPV2	BGC-Argo	Total
T/S	5 735 819	0	0	0	5 735 819
Nitrate	1 738 637	69 355	609 016	1 808 366	4 225 374
Phosphate	2 902 300	98 652	577 388	0	3 578 340
Silicate	2 252 702	73 165	606 131	0	2 931 998

framework to the station and cruise levels to address systematic inconsistencies. To ensure vertical profile reliability, any station containing more than 30 % of data points flagged during the initial screening is deemed unreliable and entirely discarded. Similarly, at the expedition level, cruises exhibiting an aggregate flag rate exceeding 40 % are excluded to prevent the propagation of systematic instrumental errors or calibration drifts. The final selection process integrates flags across this hierarchy, permanently removing any data identified as erroneous at the individual, station, or cruise stage.

The final level of our quality control protocol is specifically designed to align with the input-output structure of the multi-task learning framework. Since the reconstruction relies on physical predictors to infer biogeochemical fields, complete availability of temperature and salinity is mandatory. Therefore, we apply a strict filter to ensure that every retained nutrient observation is strictly collocated with valid, high-quality physical measurements (T and S). However, unlike single-task models that might require simultaneous observations of all target variables, our multi-task architecture allows for valid training with partial targets. To maximize data utilization, we do not require the concurrent presence of all three nutrients. Instead, any data point containing valid physical predictors and at least one valid nutrient measurement is retained. This flexible inclusion strategy allows the model to leverage a significantly larger volume of historical data – where specific nutrients might be missing – thereby enhancing the distinct feature extraction capability for each element. This inclusion strategy maximizes the volume of historical data available for training. The resulting high-quality dataset exhibits extensive global coverage spanning the period 1965–2023, with the specific spatiotemporal distribution patterns illustrated in Fig. 1.

2.5 Model development and Validation

2.5.1 Input Features

The selection of input features is designed to constrain the machine learning model with both physical principles and statistical priors. The input vector consists of three distinct categories: encoded spatiotemporal coordinates, hydrographic predictors, and climatological reference features. To preserve the continuity of the global domain and the cyclical nature of seasonality, we apply specific feature engineering techniques: spatial coordinates are transformed into spherical coordinates, and the month variable is encoded into sine and cosine components to capture the continuous seasonal cycles. A list of all input variables, along with their respective sources and resolutions, is summarized in Table 2.

Potential temperature and salinity are selected as the primary physical drivers based on the fundamental control of water mass dynamics on nutrient distributions. Oceanographic studies have long established that nutrient concentrations exhibit distinct relationships with temperature and salinity along isopycnal surfaces, enabling these hydrographic variables to serve as effective proxies for identifying distinct water masses. Consequently, utilizing collocated temperature and salinity as core predictors has become a standard practice in global biogeochemical reconstruction models (e.g., Sauzède et al., 2017; Bittig et al., 2018; Broullón et al., 2019; Keppler et al., 2020; Carter et al., 2021).

Furthermore, we incorporate six climatological variables from WOA to serve as spatial reference features. By explicitly including these mean environmental states as inputs, the neural network is guided to learn the non-linear relationships between the background hydrographic conditions and nutrient distributions. This "climatology-informed" strategy provides a stable environmental reference baseline, enhancing model stability and convergence.

To align the model inputs with observational reality, we implement a distinct data construction strategy for the training and inference phases. During the training phase, the model inputs are derived from the quality-controlled observational dataset to represent in situ conditions. Specifically, we use the in situ measured temperature and salinity, while the corresponding climatological features are obtained by linearly interpolating the standard WOA grids to the exact spatiotemporal position of each nutrient observation. In contrast, the global inference phase requires spatially continuous products to generate the full 4D reconstruction. Drawing on its established role as a robust physical forcing in historical oceanographic reconstructions (Cheng et al., 2017; Zanna et al., 2019) and large-scale biogeochemical mappings (Landschützer et al., 2016), we directly utilize the time-varying EN4 gridded fields to represent the historical hydrographic conditions. Concurrently, the WOA climatological features are drawn directly from their standard grid points. This dual strategy ensures that the model is trained on local relationships while being capable of projecting these learned patterns

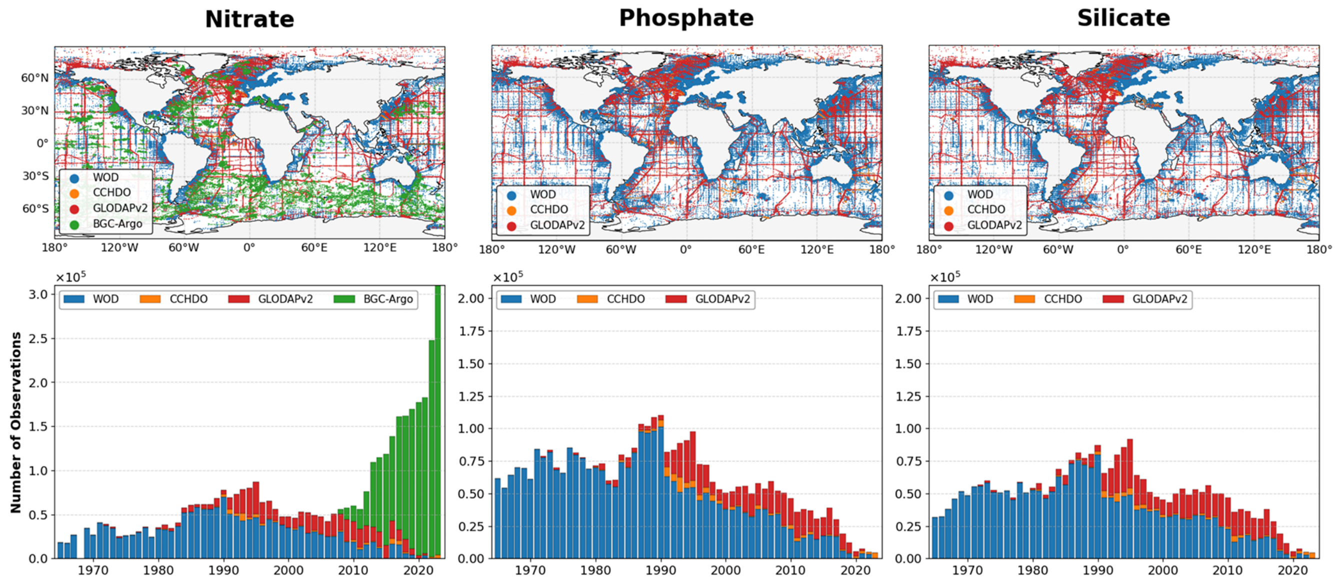

Figure 1. Spatial and temporal distribution of the nutrients data after quality control.

onto the global domain driven by spatiotemporal physical inputs.

2.5.2 Model Architecture

The operational workflow detailing the training and inference phases of the Jingwei-Nutrients model is illustrated in Fig. 2. At the core of this pipeline, to capture the complex, non-linear interactions between physical drivers and biogeochemical tracers, we employ a Transformer-based deep learning architecture. This framework, originally developed for sequence representation learning (Vaswani et al., 2017), has been recently adapted for high-dimensional Earth system modeling (e.g., Bi et al., 2023; Lam et al., 2023) and complex oceanographic field reconstructions (Reichstein et al., 2019; Sonnewald et al., 2021). The cornerstone of this architecture is the self-attention mechanism, which fundamentally distinguishes it from traditional regression models or standard convolutional networks.

Unlike static methods that treat input features independently, the self-attention mechanism dynamically calculates "attention weights" to quantify the relevance of different input features relative to one another. In the context of nutrient reconstruction, this capability allows the model to inherently learn and weigh the variable coupling strength between specific physical conditions (e.g., temperature, salinity, depth) and nutrient concentrations. By establishing these adaptive connections, the Transformer can focus on the most critical predictors for identifying distinct water masses, thereby improving prediction accuracy in spatially heterogeneous ocean environments.

Specifically, the network architecture adopts a Multi-Task Learning (MTL) framework designed to simultaneously reconstruct the three target nutrients (NO_3^-, PO_4^{3-}, and $Si(OH)_4$). The network is composed of a shared feature extraction backbone followed by three element-specific prediction heads. The input feature vector is initially processed by shared Transformer encoder layers, which are designed to capture the coupled physical-biogeochemical linkages driven by the hydrographic environment. Rather than learning isolated generic representations, these shared layers extract the concurrent stoichiometric relationships among the nutrients. Subsequently, the shared feature representations are routed into three parallel, task-specific decoding heads. Each head acts as a specialized regression module dedicated to a single element, optimizing for its unique vertical gradient and spatial distribution. Crucially, during training, the information learned by each nutrient decoding head is continuously propagated back to the shared layers. By jointly shaping the shared representation space, the MTL framework enables the joint learning of coherent biogeochemical patterns. This dynamic mutual calibration not only enhances computational efficiency through shared weights but, more importantly, provides a structural mechanism to encourage stoichiometric consistency. By sharing representations across elements, the model is inherently guided to learn their concurrent biogeochemical variations, reducing the likelihood of generating the physically divergent patterns that can arise from training independent single-task models.

2.5.3 Multi-Task Optimization Strategy

The stoichiometric ratios among marine nutrients are not globally static; rather, they exhibit pronounced variability across distinct horizontal domains, depth horizons, and temporal scales (Liu et al., 2025). Consequently, we employ

Table 2. Summary of the input variables used for the global nutrient reconstruction, including their respective data sources, temporal coverage, and spatial resolutions.

Feature name	Data source	Spatial resolution	Temporal resolution
Geographical features			
Latitude [° N]	Sampling information		
Longitude [° E]	Sampling information		
Depth [m]	Sampling information		
Oceanographic features			
Temperature [°C]	World Ocean Database 2023		
Salinity [unitless]	World Ocean Database 2023		
Dissolved oxygen [µmol kg^{-1}]	World Ocean Atlas 2023	1° × 1°	Annual climatology
Percent Oxygen Saturation [%]	World Ocean Atlas 2023	1° × 1°	Annual climatology
Apparent Oxygen Utilization [µmol kg^{-1}]	World Ocean Atlas 2023	1° × 1°	Annual climatology
Density [kg m^{-3}]	World Ocean Atlas 2018	1° × 1°	Seasonal climatology
Conductivity [S m^{-1}]	World Ocean Atlas 2018	1° × 1°	Seasonal climatology
Mixed Layer Depth [m]	World Ocean Atlas 2018	1° × 1°	Monthly climatology

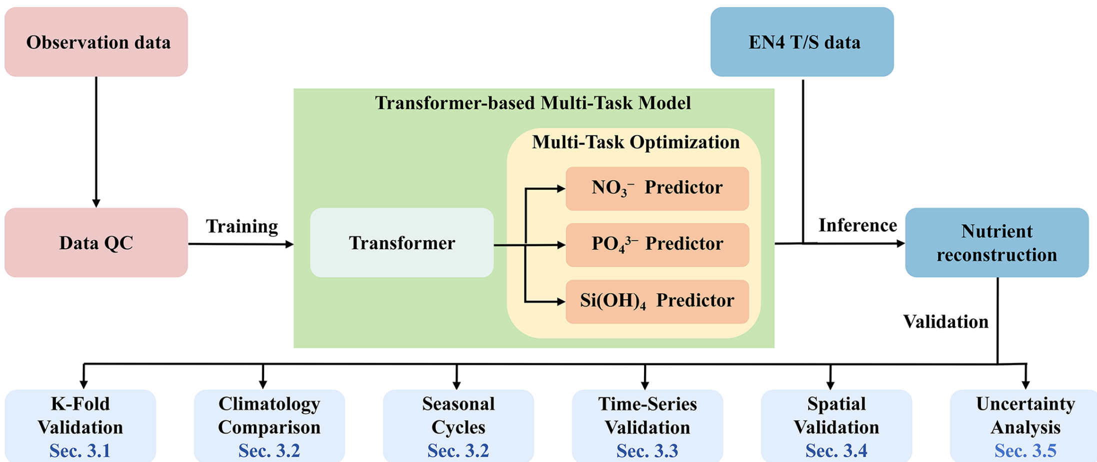

Figure 2. The overall pipeline of the Jingwei-Nutrients reconstruction framework, encompassing data preparation, the Transformer-based MTL neural network architecture, global 4D inference, and comprehensive performance validation.

a data-driven multi-task learning approach that enables the neural network to learn and represent these dynamic elemental relationships from observations within a shared latent space.

However, while this multi-task architecture enables flexible information sharing without hard-coded rules, the joint training process introduces two fundamental optimization challenges: loss scale imbalance and gradient conflict. If simply summed with equal weights, tasks with larger loss magnitudes can dominate the optimization process, while conflicting gradient directions between tasks can lead to "negative transfer" (Yu et al., 2020; Vandenhende et al., 2022), where improving the prediction of one nutrient degrades the performance of others. To address these issues and ensure balanced convergence across all biogeochemical variables, we implement a dual-strategy optimization framework.

To strictly address the optimization imbalance caused by differing variances and units among NO_3^-, PO_4^{3-}, and $Si(OH)_4$, we implement an adaptive weighting scheme based on homoscedastic uncertainty (Kendall et al., 2018). Instead of manually assigning fixed hyperparameters, this method treats the task-dependent weight as a learnable parameter derived from the inherent observation noise. The total multi-task objective function L_{total} is formulated as Eq. (1):

$$L_{\text{total}}(W\sigma_1, \ldots, \sigma_T) = \sum_{t \in \{\text{N,P,Si}\}} \left(\frac{1}{2\sigma_t^2} L_t(W) + \log \sigma_t \right), \qquad (1)$$

where $L_t(W)$ denotes the task-specific loss (MSE) for nutrient t, and σ_t represents the learnable noise parameter. In Eq. (1), the term $\frac{1}{2\sigma_t^2}$ automatically down-weights tasks with high uncertainty, while the regularization term $\log \sigma_t$ prevents the variance from increasing indefinitely, allowing the model to dynamically balance the learning focus among the three elements throughout the training process.

Furthermore, to mitigate the geometric conflicts where the gradient update for one task might detrimentally affect another, we integrate the Project Conflicting Gradients (PCGrad) algorithm (Yu et al., 2020). This strategy monitors the cosine similarity between the gradient vectors of any two tasks during backpropagation. When a conflict is detected (i.e., their dot product is negative), the gradient is projected to eliminate the destructive component, as calculated in Eq. (2):

$$\boldsymbol{g}_i^{\mathrm{PC}} = \boldsymbol{g}_i \frac{\boldsymbol{g}_i \cdot \boldsymbol{g}_j}{\left|\boldsymbol{g}_j\right|^2} \boldsymbol{g}_j, \tag{2}$$

where $\boldsymbol{g}_i$ and $\boldsymbol{g}_j$ denote the original gradient vectors for task i and task j, respectively, and $\boldsymbol{g}_i^{\mathrm{PC}}$ represents the corrected gradient for task i projected onto the normal plane of $\boldsymbol{g}_j$. By iteratively applying this projection, PCGrad mitigates inter-task gradient conflicts by suppressing destructive gradient components, thereby facilitating more balanced optimization of the shared parameters and reducing negative transfer among nutrient predictions.

2.6 Model Evaluation and Experimental Design

The reconstruction performance is quantitatively evaluated using two standard statistical metrics: the Coefficient of Determination (R^2) and Root Mean Square Error (RMSE). Let N denote the total number of matched samples, while $y_{\mathrm{obs},i}$ and $y_{\mathrm{pred},i}$ represent the observed and predicted values for the ith sample, respectively, and $\bar{y}_{\mathrm{obs}}$ is the mean of the observed values. These metrics are calculated as follows:

$$R^2 = 1 - \frac{\sum_{i=1}^{N} (y_{\mathrm{obs},i} - y_{\mathrm{pred},i})^2}{\sum_{i=1}^{N} (y_{\mathrm{obs},i} - \bar{y}_{\mathrm{obs}})^2}, \tag{3}$$

$$\mathrm{RMSE} = \sqrt{\frac{1}{N} \sum_{i=1}^{N} (y_{\mathrm{obs},i} - y_{\mathrm{pred},i})^2}, \tag{4}$$

To evaluate the model's performance and the effects of the proposed architecture, we design a rigorous training and comparative framework. We adopt a strict time-based K-fold cross-validation strategy to prevent temporal data leakage. In this study, $K = 6$, and the 59-year dataset is divided into six chronological folds: 1965–1975, 1976–1985, 1986–1995, 1996–2005, 2006–2015, and 2016–2023. By partitioning the 59-year dataset into chronological blocks rather than random subsets, distinct time periods are rigorously isolated as test sets, providing an objective assessment of the model's generalization. Within this cross-validation framework, we further establish a comparative baseline by training independent Single-Task Learning (STL) models for each nutrient. Comparing the proposed multi-task framework against these single-element counterparts under identical conditions allows us to verify the mutual enhancement effects driven by shared feature learning.

Beyond statistical benchmarks, a multi-dimensional verification scheme is implemented to assess the physical and biogeochemical representation of the reconstruction. This comprehensive evaluation includes: (1) Climatological Patterns and Seasonal Cycles, which examines the reproduction of large-scale seasonal variations and long-term trends; (2) Temporal Dynamics through Station Validation, where representative stations are selected to evaluate the time-series dynamics and vertical profiles; (3) Spatial Variability through Cruise Verification, utilizing independent cruise data to assess the spatial representation of nutrient distributions across ocean basins; and (4) Spatiotemporal Uncertainty Analysis, which quantifies the model variance and uncertainties of the reconstructed product across different oceanic regions and historical periods.

To ensure independent station and cruise-section validations, all HOT, KERFIX, P16N (2015), P16S (2014), and P06E (2017) observations are excluded from the training data before model development, including duplicate or overlapping records in the source archives. These reserved observations are identified using station information, cruise identifiers, and spatiotemporal coordinates, and are used only for the validations described in Sect. 3.3 and 3.4. Detailed results and analyses from these validation modules are presented in Sect. 3.

3 Results

3.1 Model Performance

The reconstruction performance of the proposed Multi-Task Learning (MTL) and Single-Task Learning (STL) models is evaluated using aggregated predictions from the validation sets of the time-based K-fold cross-validation. Figure 3 presents the density scatter plots comparing the reconstructed nutrient concentrations against the in situ observations across the full study period (1965–2023) for both architectures. By utilizing chronological blocking rather than random partitioning, the evaluation mitigates the influence of short-term temporal persistence, providing an objective assessment of the models' generalization capabilities. The scatter distributions for both the MTL and STL models generally align with the 1 : 1 reference line across the concentration spectrum, indicating that the models can reproduce the concentration limits without systematic bias. Furthermore, a comparison of the scatter distributions reveals that the MTL model shows tighter alignment with the reference line than the STL model, demonstrating improved reconstruction performance for all three nutrients.

Table 3 summarizes the quantitative metrics (R^2 and RMSE) to further assess the specific effects of the multi-task architecture compared to the single-task baselines. On aver-

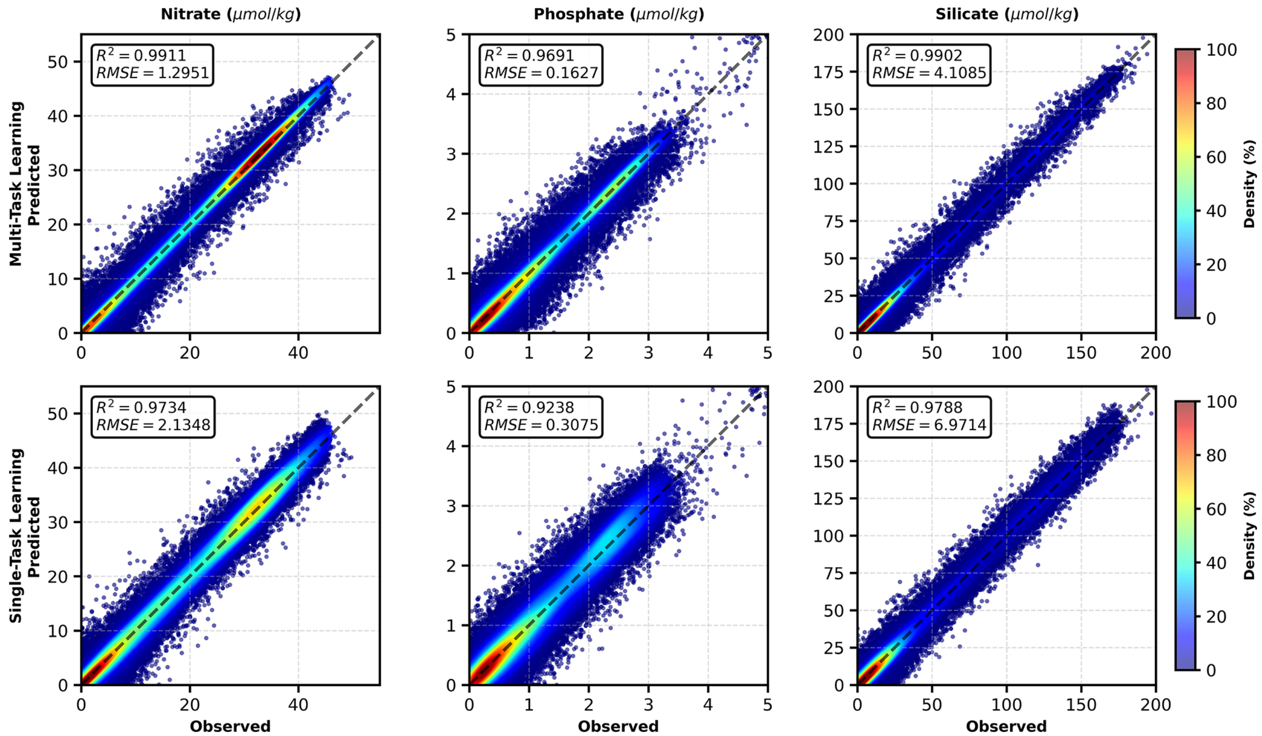

Figure 3. Density scatter plots comparing the Jingwei-Nutrients reconstructed concentrations against in situ observations for nitrate, phosphate, and silicate. The plots aggregate all matched test samples from the strict time-based K-fold cross-validation over the entire study period (1965–2023). Colors indicate the density of data points, and the dashed line represents the 1 : 1 ideal agreement.

age, the MTL framework yields R^2 values of 0.9911, 0.9691, and 0.9902 for nitrate, phosphate, and silicate, respectively, with corresponding mean RMSE values of 1.2951, 0.1627, and 4.1085. As shown in Table 3, the joint learning framework consistently yields lower RMSE and higher R^2 values compared to the single-element models across all chronological folds. Overall, the MTL approach reduces the fold-averaged RMSE by approximately 39.3 % for nitrate, 47.1 % for phosphate, and 41.1 % for silicate compared with their STL counterparts. This improvement can be attributed to the shared representation mechanism of the MTL architecture. By processing the elements jointly, the model is guided to learn their concurrent biogeochemical variations, which contributes to the observed improvements in numerical accuracy compared to the isolated single-task models.

Beyond the performance differences between the two architectures, a common characteristic observed in both the MTL and STL results is a progressive improvement in predictive performance from the 1960s to the 2020s. For instance, the MTL RMSE for nitrate decreases from 1.8306 in the 1965–1975 fold to 0.9273 in the 2016–2023 fold. This temporal trend corresponds with the historical evolution of global ocean observing systems; the relatively higher errors in earlier decades relate to the spatial sparsity of historical bottle measurements, whereas recent accuracy gains reflect the availability of high-density hydrographic observations that provide additional physical constraints for the models.

3.2 Climatological Patterns and Seasonal Cycles

To evaluate whether the Jingwei-Nutrients data product captures the fundamental biogeochemical structure of the global ocean, we compare the model-derived climatologies with the standard World Ocean Atlas 2023 (WOA23). This comparison assesses whether the Jingwei-Nutrients model captures large-scale spatial patterns rather than overfitting to local observations. Figures 4 to 6 display the comparison of spatial distributions for nitrate, phosphate, and silicate across three representative depth layers: the surface (0 m), the intermediate layer (500 m), and the deep layer (2000 m). Overall, the reconstructed fields show spatial agreement with WOA23, reproducing the major global nutrient regimes across these selected depths.

The spatial patterns at each evaluated stratum reflect distinct physical-biogeochemical dynamics. As illustrated in Fig. 4, at the surface layer (0 m), the model reproduces the global nutrient regimes governed by biological uptake and physical stratification, identifying the nutrient-depleted oligotrophic subtropical gyres alongside the High-Nutrient Low-Chlorophyll (HNLC) outcropping in the Southern Ocean (Moore et al., 2013). At the intermediate layer (500 m) in

Table 3. Statistical evaluation metrics (R^2 and RMSE) of the chronological K-fold cross-validation. The results highlight the decadal performance evolution and compare the predictive accuracy of the MTL architecture against independent STL models for nitrate, phosphate, and silicate reconstructions. The unit for all RMSE values is µmol kg^{-1}.

	Multi-Task Learning						Single-Task Learning					
Fold	N (R^2/RMSE)		P (R^2/RMSE)		Si (R^2/RMSE)		N (R^2/RMSE)		P (R^2/RMSE)		Si (R^2/RMSE)	
1965–1975	0.9847	1.8306	0.9476	0.1986	0.9794	6.1854	0.9618	3.1264	0.8967	0.4177	0.9605	9.1755
1976–1985	0.9865	1.5452	0.9430	0.2094	0.9834	4.7658	0.9651	2.6278	0.8908	0.4080	0.9672	8.8442
1986–1995	0.9889	1.3298	0.9618	0.1688	0.9881	4.1327	0.9694	2.2483	0.9146	0.3368	0.9753	7.7289
1996–2005	0.9937	1.1494	0.9831	0.1501	0.9958	3.5784	0.9781	1.9364	0.9415	0.2586	0.9883	5.8910
2006–2015	0.9955	0.9883	0.9863	0.1327	0.9968	3.1057	0.9813	1.5911	0.9455	0.2394	0.9900	5.3172
2016–2023	0.9974	0.9273	0.9928	0.1166	0.9977	2.8830	0.9847	1.2788	0.9537	0.1845	0.9915	4.8716
Avg	0.9911	1.2951	0.9691	0.1627	0.9902	4.1085	0.9734	2.1348	0.9238	0.3075	0.9788	6.9714

Fig. 5, the spatial patterns transition to reflect organic matter remineralization and main thermocline ventilation, mapping the accumulation of regenerated nutrients in the North Pacific and Indian Ocean oxygen minimum zones (OMZs) (Paulmier and Ruiz-Pino, 2009; Sarmiento and Gruber, 2006). In the deep layer (2000 m), as shown in Fig. 6, the reconstruction captures the large-scale horizontal gradients associated with the global thermohaline circulation. The spatial distribution aligns with the general nutrient accumulation pattern (Broecker, 1991), transitioning from the relatively nutrient-poor North Atlantic Deep Water (NADW) to the older, nutrient-rich Pacific Deep Water (PDW) (Sarmiento and Gruber, 2006).

The difference maps between the reconstructed fields and WOA23 provide further insight into the spatial distribution of residuals. While the anomalies are generally small across open-ocean basins, their spatial and vertical distributions exhibit structured patterns. Spatially, larger deviations are primarily located in high-latitude regions (e.g., the Southern Ocean) and certain coastal margins. Vertically, the differences in the shallow euphotic layers tend to be larger than those in the deep ocean. This spatial-vertical contrast aligns with established oceanographic processes: surface waters and high-latitude regimes are modulated by seasonal biological uptake, atmospheric forcing, and mesoscale dynamics (Benitez-Nelson et al., 2007; Moore et al., 2013), introducing greater natural variability. In contrast, the deep ocean is characterized by relatively stable, slow-moving water masses driven by large-scale circulation. Overall, these regional variations are consistent with known oceanographic processes, and the comparison indicates that the Jingwei-Nutrients product provides a consistent representation of global biogeochemical distributions.

The vertical representation of the reconstructed fields is examined by comparing meridional sections across distinct ocean basins. Figures 7 and 8 present the vertical distributions of nitrate, phosphate, and silicate along two representative lines: 25° W in the Atlantic Ocean and 90° E in the Indian Ocean. The reconstructed fields capture the basin-scale fractionation patterns associated with the global thermohaline circulation. As illustrated in Fig. 7, the Atlantic sector exhibits relatively lower nutrient concentrations, showing the southward-intruding tongue of the ventilated, nutrient-poor North Atlantic Deep Water (NADW) in the mid-to-deep layers. Conversely, Fig. 8 displays the transition to higher deep-water concentrations in the Indian Ocean interior, reflecting the accumulation of remineralized organic matter along the aging path of the deep circulation (Broecker, 1991; Sarmiento and Gruber, 2006). Across both basins, the characteristic vertical gradient – rapid nutrient depletion in the euphotic zone followed by an increase across the thermocline to a deep maximum – is evident, indicating that the reconstruction captures the vertical coupling associated with the biological pump and subsequent subsurface remineralization (Sigman and Hain, 2012).

The difference maps in the rightmost columns of Figs. 7 and 8 provide further details on the distribution of residuals within the ocean interior. Anomalies are generally small across the majority of the water column. However, larger deviations are primarily localized along the boundaries of major water masses and in regions characterized by sharp spatial gradients. For instance, higher differences are observed around the edges of the NADW nutrient tongue and across the stratified main thermocline. This distribution of differences is physically interpretable, as these transition zones feature intense mixing and dynamic frontogenesis, introducing greater natural variability. Furthermore, the observed differences at these complex physical-biogeochemical interfaces may partially arise from distinct methodological approaches. While traditional objective analysis relies on spatial autocorrelation, the data-driven model infers nutrient concentrations through non-linear relationships with varying physical drivers. Overall, these comparisons indicate that the Jingwei-Nutrients data product provides a structurally consistent representation of three-dimensional biogeochemical distributions.

Beyond static spatial patterns, the temporal evolution of nutrient fields is critical for understanding ecosystem dy-

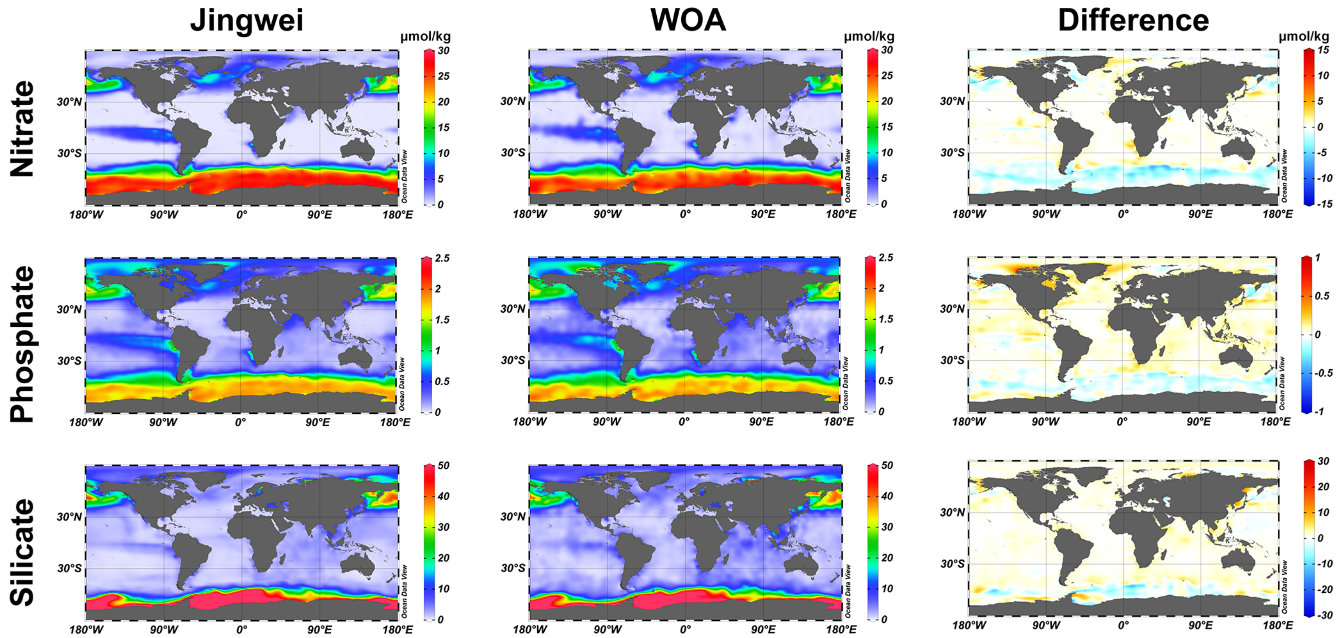

Figure 4. Spatial comparison of the climatological mean distributions of nitrate, phosphate, and silicate at the sea surface (0 m). The left column displays the Jingwei-Nutrients reconstruction, the middle column shows the WOA23 standard reference, and the right column presents the absolute difference (Jingwei minus WOA23). The surface fields highlight the model's effective capture of nutrient-depleted subtropical gyres and nutrient-rich outcropping zones.

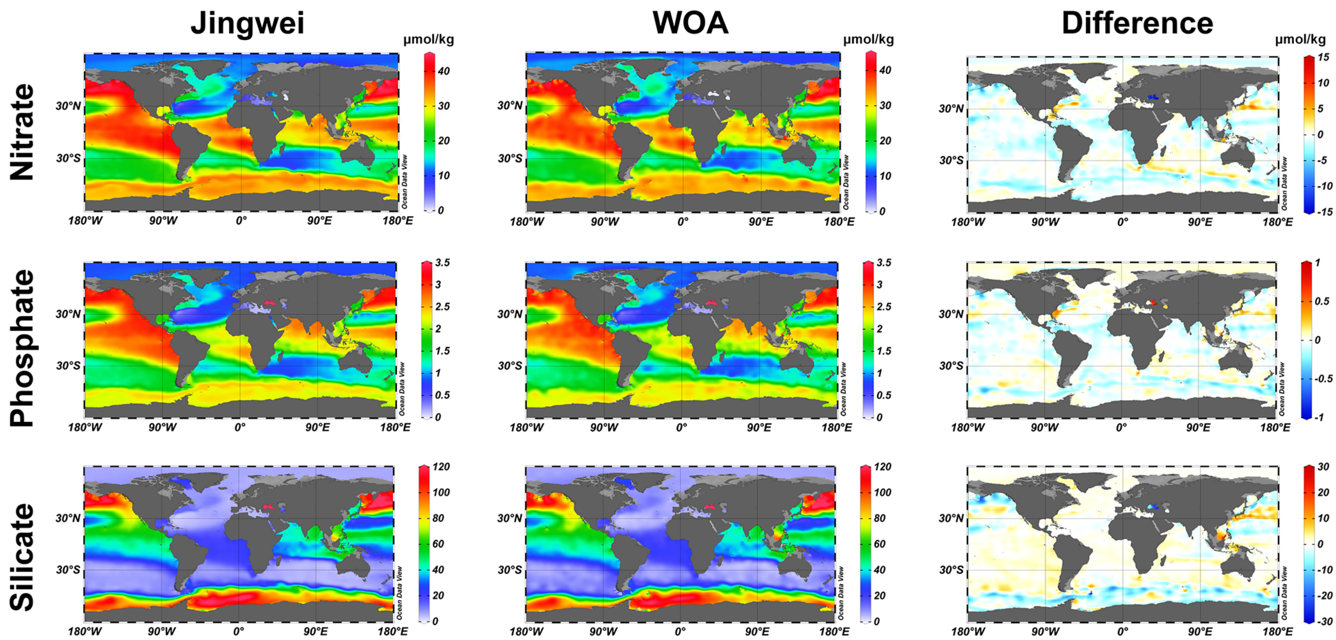

Figure 5. The Global climatological distributions of nitrate, phosphate, and silicate at the intermediate layer (500 m). The column and row layout is identical to Fig. 4.

namics and phenology (Longhurst, 2007). Figure 9 compares the reconstructed seasonal anomaly cycles with WOA23 data across the Northern and Southern Hemispheres at four representative depths (0, 50, 300, and 800 m). The Jingwei-Nutrients reconstruction (solid lines) aligns with the WOA23 reference (dashed lines), capturing both the phase and amplitude of the seasonal variations. The model reproduces the out-of-phase seasonal dynamics between the two hemispheres. In the biologically active shallow layers (0 and 50 m), a pronounced seasonal amplitude is evi-

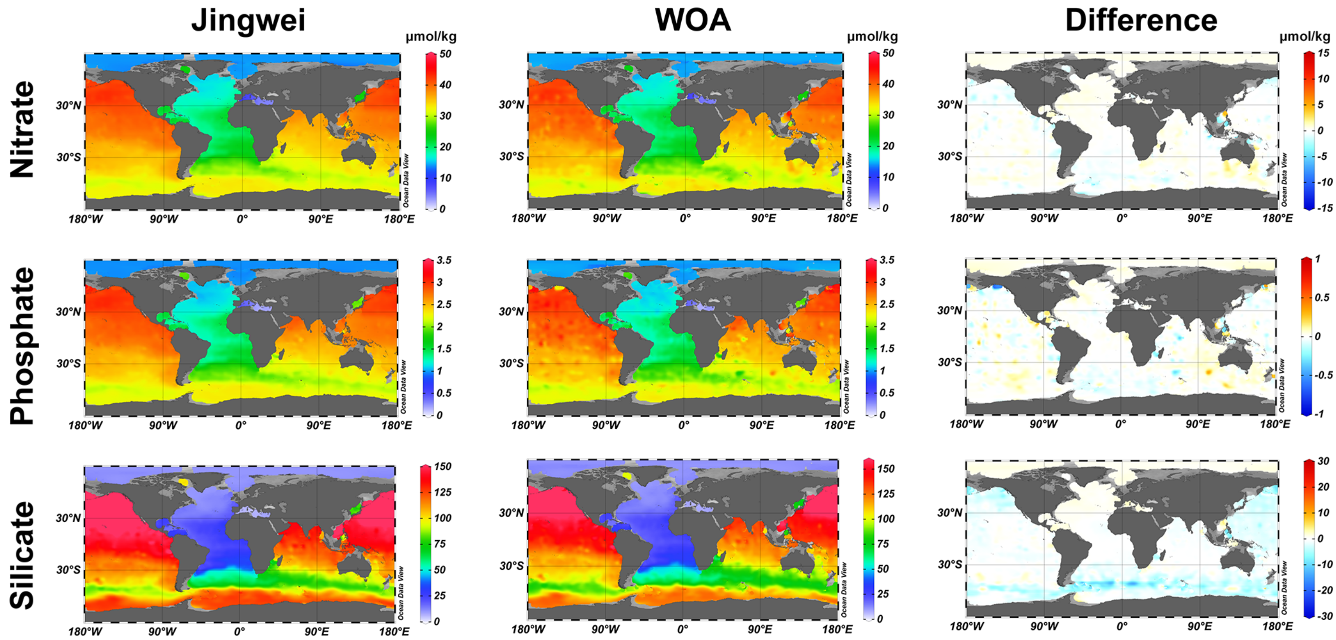

Figure 6. Global climatological distributions of nitrate, phosphate, and silicate at the deep layer (2000 m). The column and row layout is identical to Fig. 4.

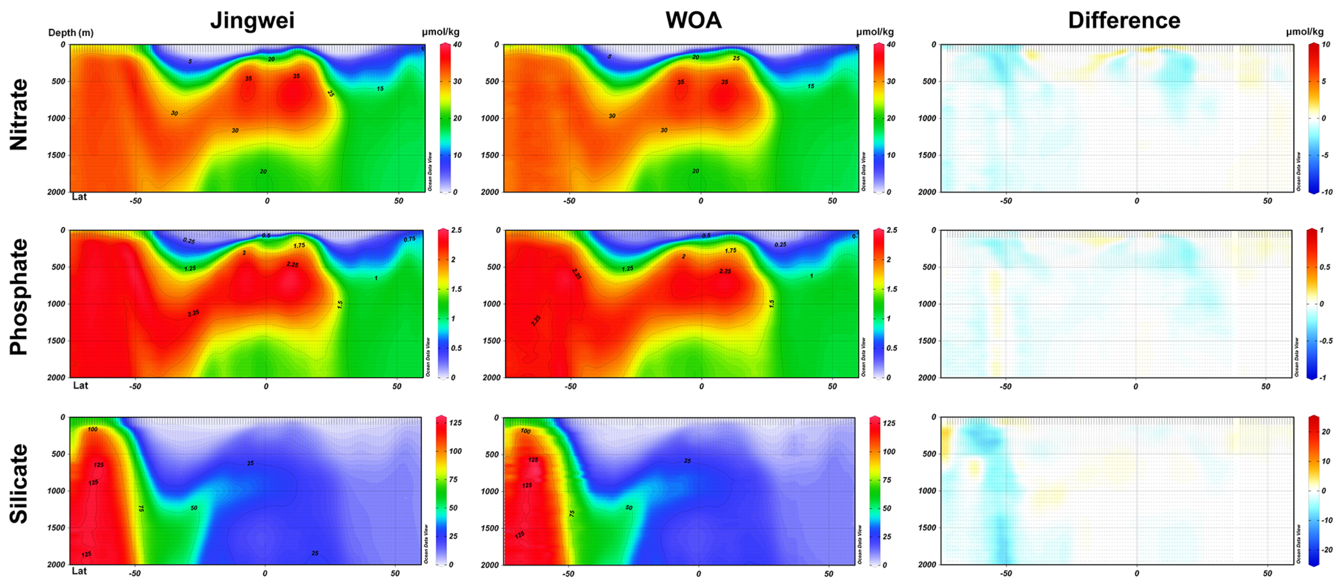

Figure 7. Vertical distribution of climatological mean nutrients along the 25° W meridional section in the Atlantic Ocean.The left column presents the Jingwei-Nutrients reconstruction, the middle column displays the WOA23 standard reference, and the right column shows the absolute difference (Jingwei minus WOA23). Rows from top to bottom correspond to nitrate, phosphate, and silicate, respectively. Units for all concentrations and differences are μmol kg^{-1}.

dent: the Northern Hemisphere shows winter/spring replenishment (January–March) mediated by convective mixing, followed by a distinct summer/autumn drawdown (July–October) driven by phytoplankton blooms (Behrenfeld et al., 2006; Keppler et al., 2020), while the Southern Hemisphere mirrors this pattern to reflect austral seasonality. Furthermore, the reconstruction captures the vertical attenuation of seasonal variability. While the euphotic zone experiences significant temporal fluctuations, the seasonal anomalies at deeper layers (300 and 800 m) are thermodynamically and biologically dampened, maintaining stable, near-zero baseline fluctuations throughout the year (Talley, 2013). This tempo-

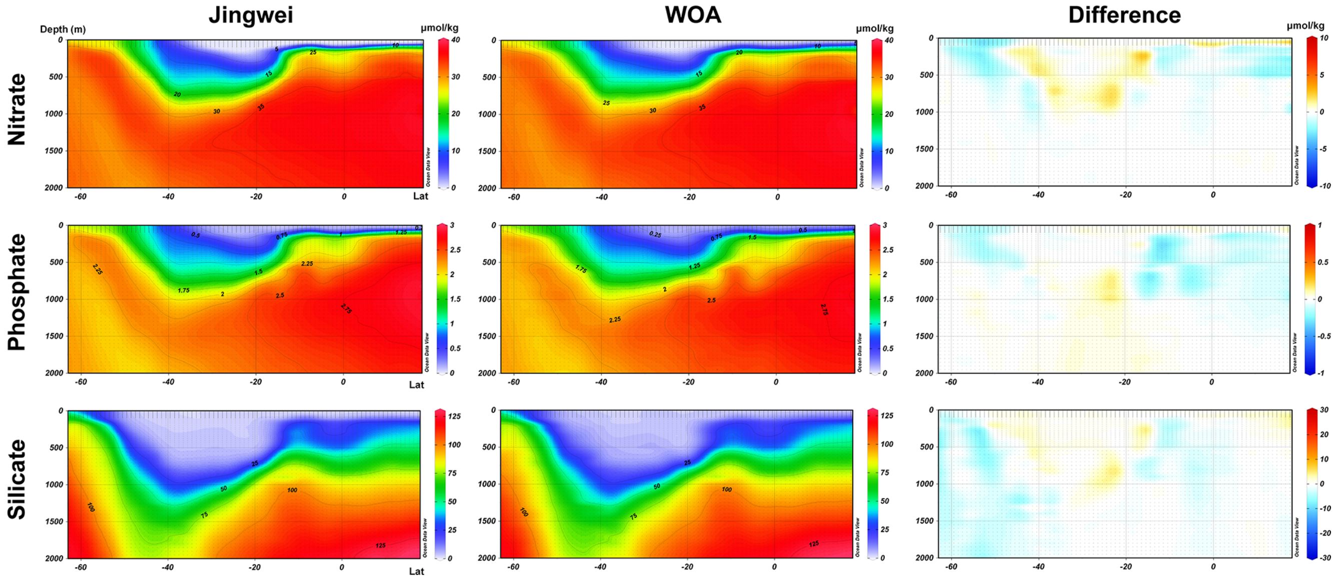

Figure 8. Vertical distribution of climatological mean nutrients along the 90° E meridional section in the Indian Ocean. The panel layout and represented variables are identical to those in Fig. 7. Units for all concentrations and differences are µmol kg^{-1}.

ral agreement indicates that the Jingwei-Nutrients data product captures the phenological timing of global biogeochemical cycles.

3.3 Temporal Dynamics through Station Validation

To assess the reproduction of localized biogeochemical variability, we perform independent validations using in situ observations from two globally representative, long-term ecological time-series stations. These observatories encompass distinct marine biogeochemical regimes: the Hawaii Ocean Time-series (HOT; Karl and Lukas, 1996), which represents the highly stratified, oligotrophic subtropical gyre of the North Pacific; conversely, the KERFIX station (Jeandel et al., 1998) in the Southern Ocean represents a dynamic, high-latitude regime dominated by deep convective winter mixing and intense seasonal blooms. The HOT and KERFIX observations used in this evaluation are excluded from the training data and retained only for independent station validation.

Figure 10 presents the evaluations for the HOT station. The Jingwei-Nutrients data product shows consistent agreement with observations. As shown in the scatter plots, the predicted concentrations at the HOT station (Fig. 10) tightly cluster around the 1 : 1 reference line, yielding high localized correlation coefficients ($R^2 \geq 0.993$) and low RMSE (1.34, 0.11, and 3.32 µmol kg^{-1} for nitrate, phosphate, and silicate, respectively). The vertical profile comparisons reveal that the product delineates the depth-dependent biogeochemical gradients, capturing the stably depleted surface layers and the depth of the deep nutricline at this location. Furthermore, for the interannual time-series comparisons, we select depth layers characterized by abundant historical observations and high biogeochemical representativeness – specifically, the 300 m layer for HOT. The temporal trajectories at this specific depth demonstrate that the reconstructed fields maintain long-term stable baselines. Notably, while the historical discrete observations occasionally exhibit localized high-frequency noise or sampling-induced spikes, the continuous reconstruction smooths these short-term variations while preserving the primary physical and biological signals.

Figure 11 illustrates the validation at the KERFIX station, which represents the complex dynamics of the Southern Ocean. The time-series trajectory at the surface (0 m) indicates that the product captures pronounced seasonal amplitudes driven by winter overturning and subsequent summer biological drawdowns. At this station, the model yields high R^2 values for nitrate ($R^2 = 0.904$) and silicate ($R^2 = 0.967$), indicating that it captures the complex regional water mass mixing processes, such as the upwelling of Circumpolar Deep Water (CDW) (Talley, 2013). However, a relatively lower correlation is observed for phosphate ($R^2 = 0.749$). This specific discrepancy can be attributed to two factors. First, the absolute background concentration of surface phosphate is naturally low, which reduces the signal-to-noise ratio in historical observations and mathematically amplifies the penalty of analytical errors on the R^2 metric. Second, the intense iron limitation characteristic of the Southern Ocean (Boyd et al., 2007; Moore et al., 2013) often triggers localized decoupling of the classical N : P uptake ratio (Deutsch and Weber, 2012), a highly specific regional anomaly that poses a generalization challenge for global-scale reconstructions. Nevertheless, despite the lower R^2, the absolute error for phosphate at KERFIX remains low (RMSE = 0.14 µmol kg^{-1}). This suggests that, even in

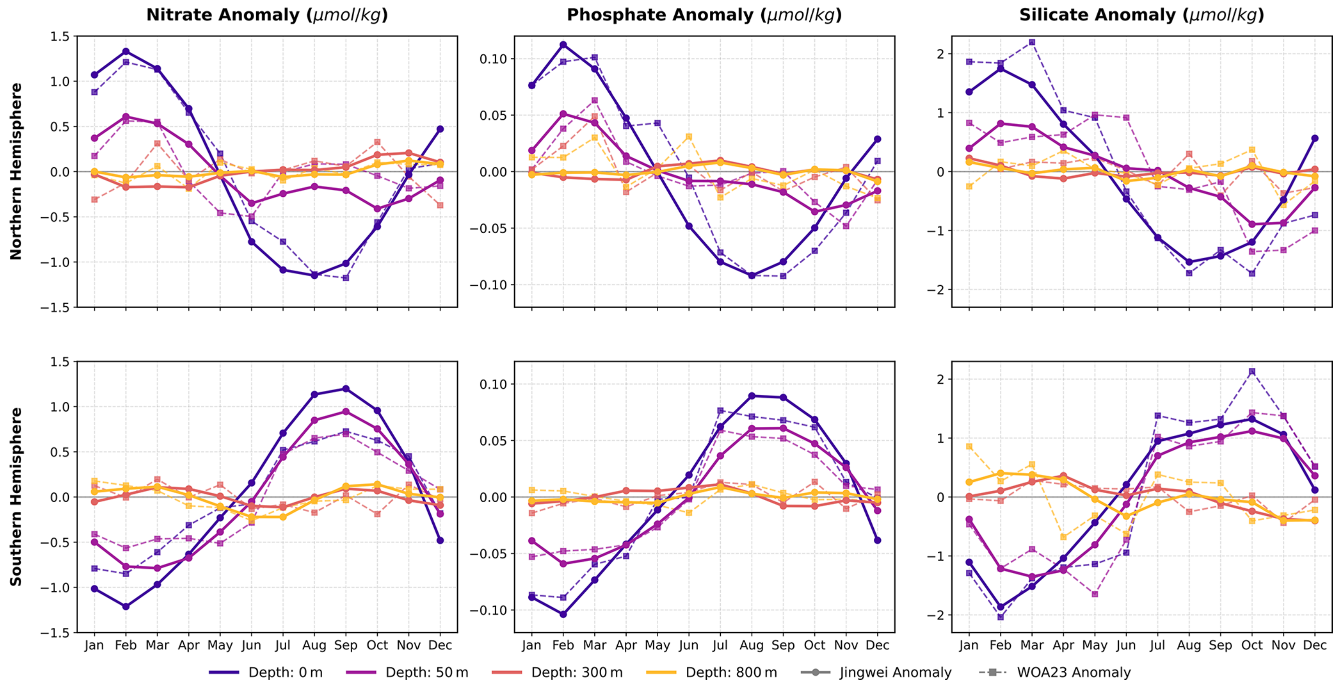

Figure 9. Seasonal cycles of nutrient anomalies across different hemispheres and depth layers. Solid lines indicate the Jingwei-Nutrients reconstruction, and dashed lines represent the WOA23 reference. The top row shows the Northern Hemisphere, and the bottom row shows the Southern Hemisphere, encompassing nitrate, phosphate, and silicate (from left to right) at 0, 50, 300, and 800 m depths. Units are μmol kg^{-1}.

dynamically complex and anomalous oceanic regimes, the Jingwei-Nutrients product provides a reliable basis for large-scale climatological and temporal analyses.

3.4 Spatial Variability through Cruise Verification

Complementing the temporal validations, capturing the three-dimensional spatial variability of the ocean interior is equally critical. To assess the spatial representation of the Jingwei-Nutrients product, we conduct independent validations using high-resolution, synoptic shipboard measurements from the U.S. GO-SHIP program (Sloyan et al., 2019). Unlike gridded climatologies that tend to smooth out transient features, continuous cruise sections provide a "snapshot" of the product's ability to reconstruct sharp frontal zones and mesoscale variabilities. As illustrated in Fig. 12, we select three representative expedition datasets encompassing different spatial domains: the P16S (2014) and P16N (2015) cruises, which together form a nearly complete meridional corridor across the Pacific Ocean, and the P06E (2017) cruise, which provides a zonal cross-section across the South Pacific. The P16N, P16S, and P06E observations used in this evaluation are excluded from the training data and retained only for independent cruise-section validation.

To facilitate a direct spatial assessment, the dense in situ measurements are objectively interpolated to construct continuous observational sections. These reference fields are then compared against the coincident cross-sections extracted from the Jingwei-Nutrients product. Figure 13 presents the comparative contour sections and the corresponding residual error distributions for the P16N cruise in the North Pacific. The reconstructed fields reproduce the large-scale accumulation of nutrients in the deep North Pacific, exhibiting high concentrations in the deep interior. The difference maps in the rightmost column reveal that deviations for nitrate and phosphate are predominantly concentrated in the 200–500 m depth range. This depth directly coincides with the stratified main nutricline, where concentrations change rapidly over short vertical distances. For silicate along this same section, larger residuals emerge deeper in the water column below 1000 m. This specific pattern is biogeochemically consistent with the complex accumulation of dissolved silica in the oldest North Pacific Deep Water, where slow biogenic dissolution processes (Tréguer et al., 2018) contribute to larger absolute variations.

Moving to the Southern Hemisphere, Fig. 14 presents the validation along the P16S section. Here, the reconstruction captures the nutrient outcropping near the Southern Ocean surface. However, the difference maps reveal a distinct error structure compared to the North Pacific. A vertical band of higher anomalies spanning from the surface to the deep ocean is visible around 45 to 50° S across all three nutrients. This localized feature corresponds to the Subantarctic Front within the Antarctic Circumpolar Current system. This dynamic region is characterized by energetic mesoscale eddies, intense deep vertical mixing, and steeply sloping isopy-

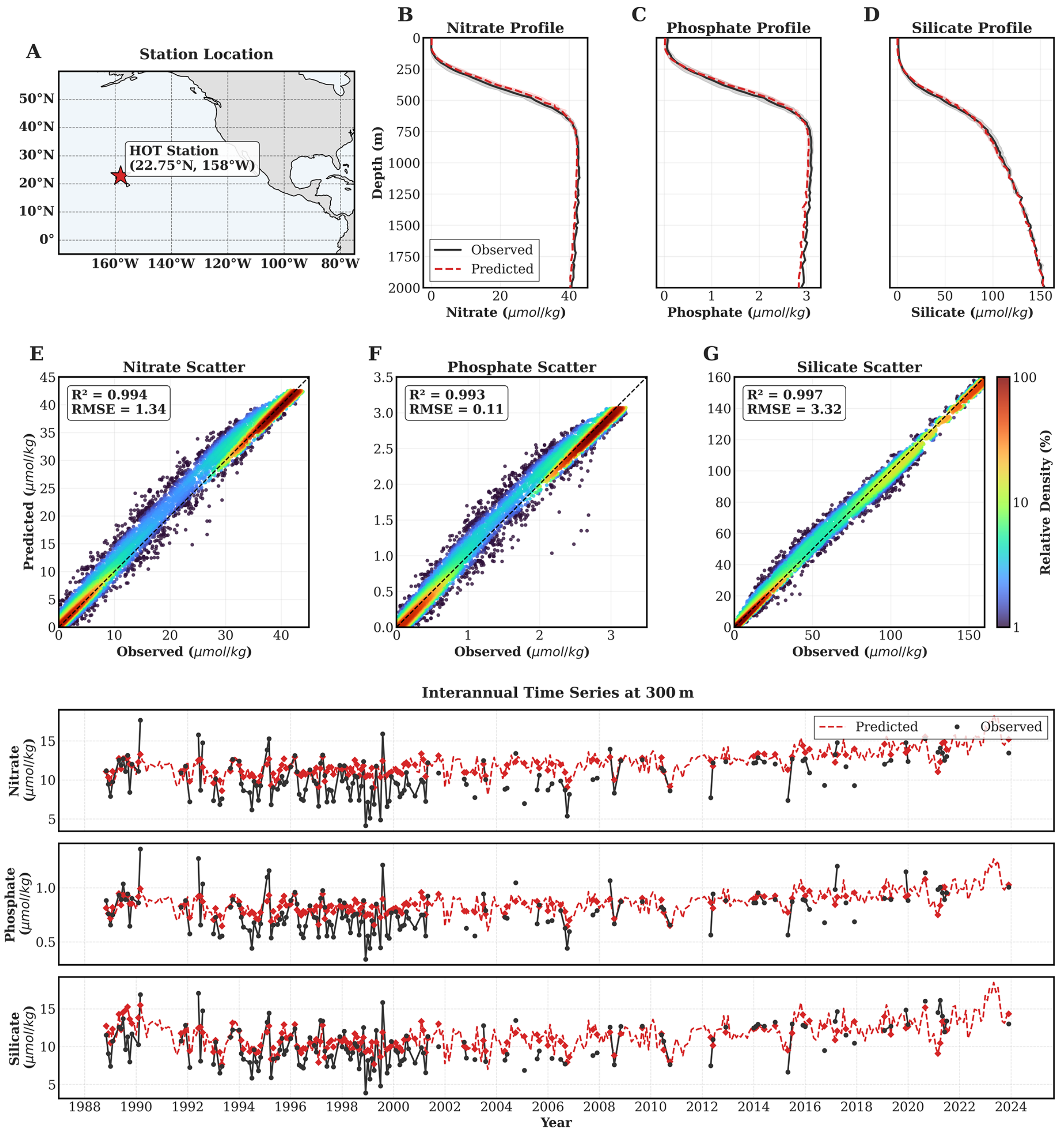

Figure 10. Multi-scale temporal and vertical validation at the Hawaii Ocean Time-series (HOT) station in the North Pacific. **(A)** Geographical location of the HOT station. **(B–D)** Climatological vertical profiles comparing in situ observations (black solid lines) and Jingwei-Nutrients predictions (red dashed lines) for nitrate, phosphate, and silicate. **(E–G)** Density scatter plots evaluating the overall predictive accuracy, with R^2 and RMSE metrics embedded. The bottom panels display the interannual time series of nutrient concentrations evaluated at the 300 m depth layer, demonstrating the model's capability to maintain stable, long-term baselines.

cnals (Marshall and Speer, 2012), creating substantial synoptic variability in the cruise "snapshot" that naturally deviates from the temporally averaged representation of a global product.

The zonal P06E section presented in Fig. 15 illustrates the east-west biogeochemical asymmetry across the South Pacific. The reconstructed cross-section captures the nutrient-rich upwelling signals, with concentration contours shoaling towards the South American eastern boundary, which is consistent with the cruise data. Moreover, the difference maps for this zonal section show low anomalies in the deep ocean interior, yielding minimal residuals below 1000 m across the entire basin. Deviations are primarily confined to the upper water column, driven by the coastal upwelling systems (Chavez and Messié, 2009).

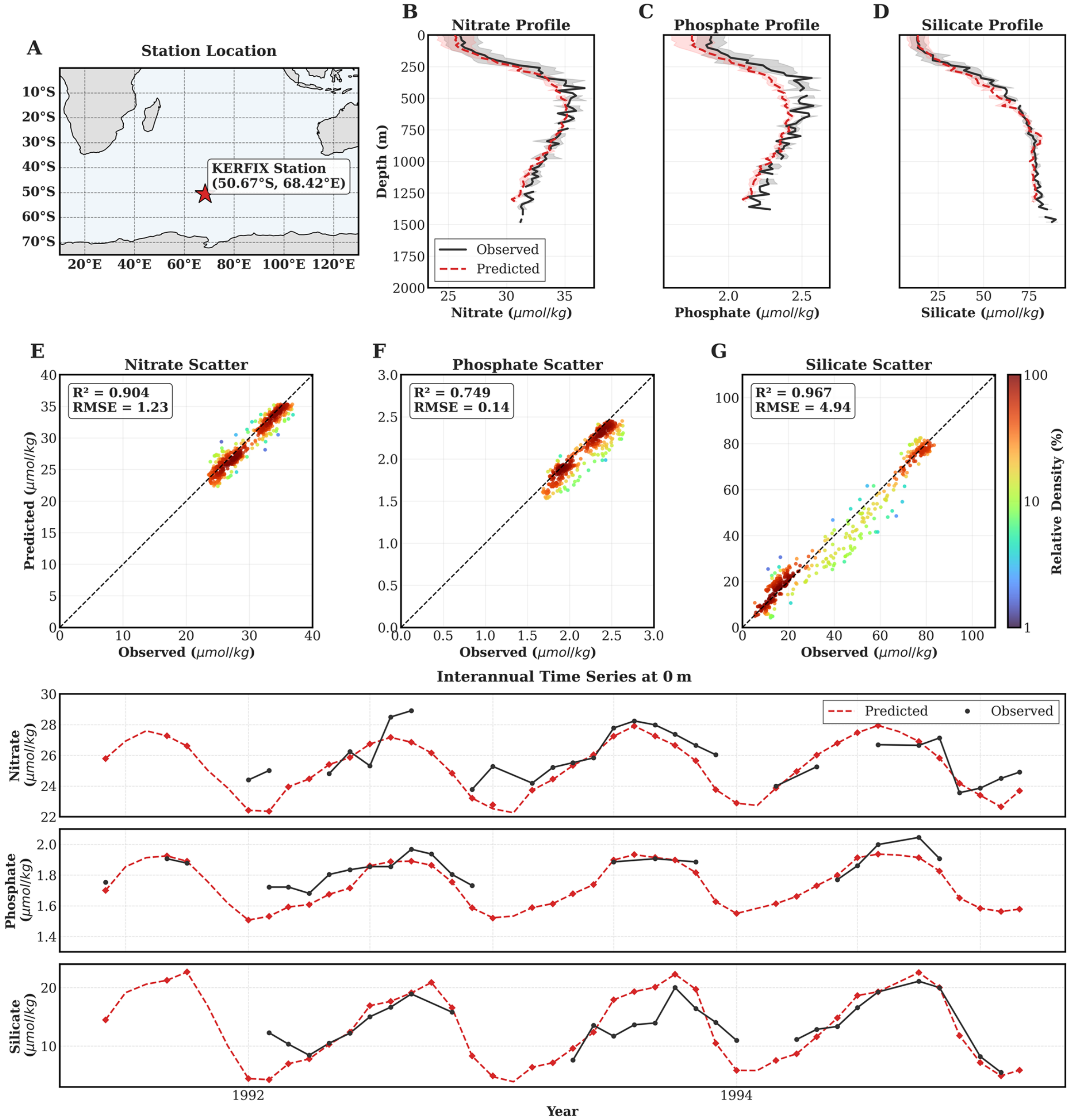

Figure 11. Multi-scale temporal and vertical validation at the KERFIX station in the Southern Ocean. The panel layout is identical to Fig. 10. This figure highlights the model's performance in a highly dynamic, high-latitude regime. The interannual time series (bottom panels) are evaluated at the surface layer (0 m) to explicitly track the massive seasonal amplitudes driven by deep convective winter mixing and summer biological drawdowns.

In summary, the cruise verification supports the three-dimensional spatial representation of the Jingwei-Nutrients product. By reproducing the synoptic features of these oceanographic sections across diverse dynamical regimes, the product demonstrates its capacity to reconstruct the continuous, full-depth spatial structure of global marine nutrients. The representation of deep-basin accumulations indicates that Jingwei-Nutrients provides a physically consistent global product.

3.5 Spatiotemporal Uncertainty Analysis

To systematically evaluate the reliability of the Jingwei-Nutrients product, it is essential to quantify its spatiotemporal uncertainty. Since mapping sparse data often introduces more uncertainty than inherent measurement errors (Ito et al., 2025), relying solely on analytical errors is inadequate. Instead, we estimate reconstruction uncertainty using the ensemble standard deviation (SD) across our six K-fold models (Gregor et al., 2019). As shown in Fig. 16, this ensemble

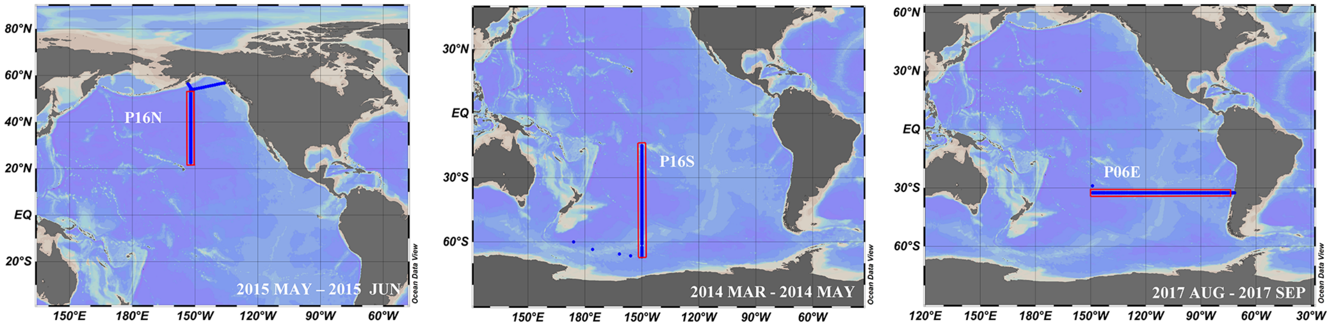

Figure 12. Map of the selected U.S. GO-SHIP cruise trajectories used for independent spatial validation. The solid lines indicate the continuous high-resolution shipboard measurement sections: the P16N (2015) and P16S (2014) meridional cruises in the Pacific Ocean, and the P06E (2017) zonal cruise in the South Pacific.

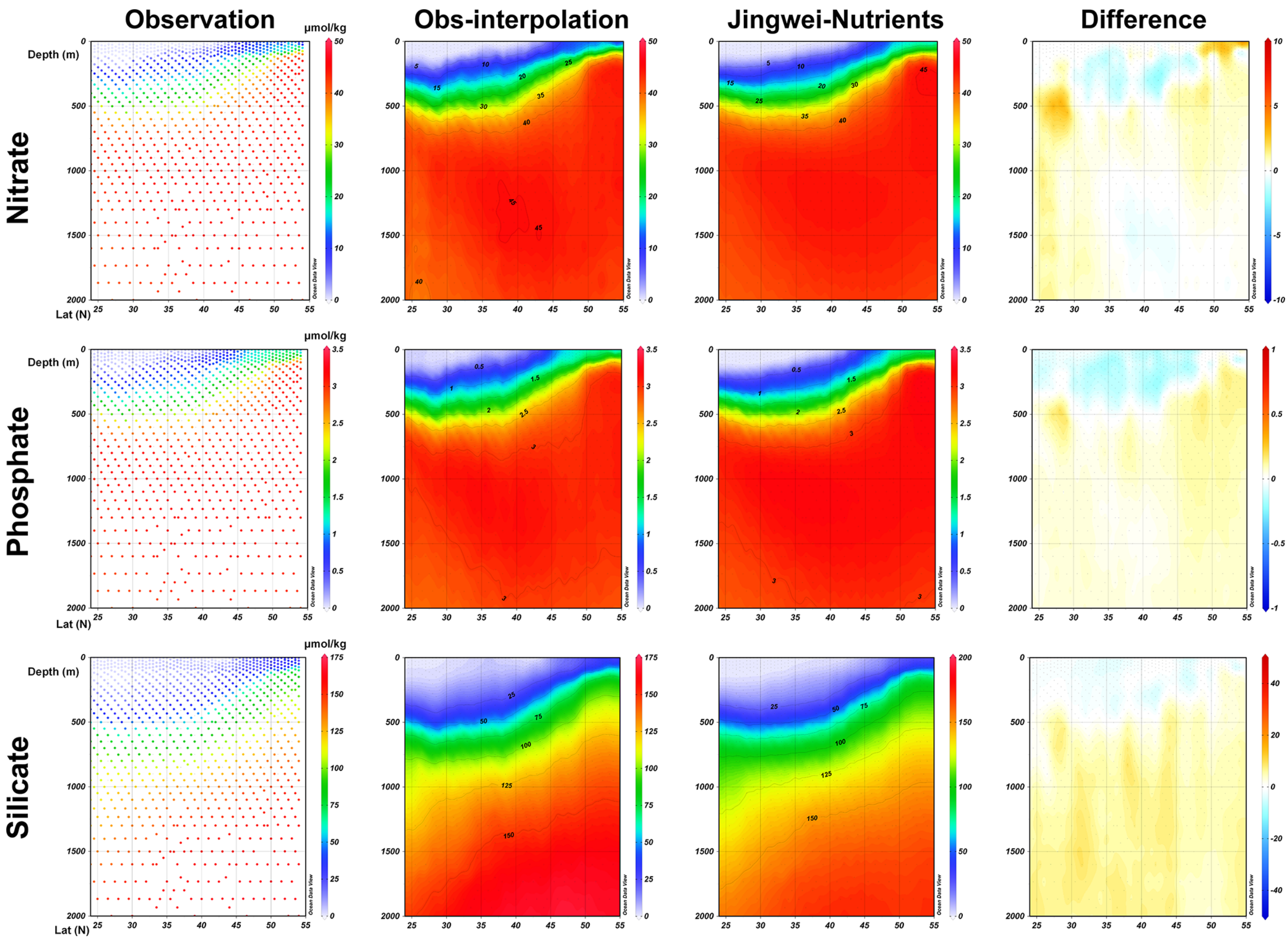

Figure 13. Spatial validation of nutrients along the P16N meridional section in the North Pacific. Columns from left to right display the in situ discrete shipboard measurements, the objectively interpolated observational field, the coincident cross-section extracted from the Jingwei-Nutrients product, and the absolute difference (Jingwei minus Observation). Rows from top to bottom correspond to nitrate, phosphate, and silicate, respectively.

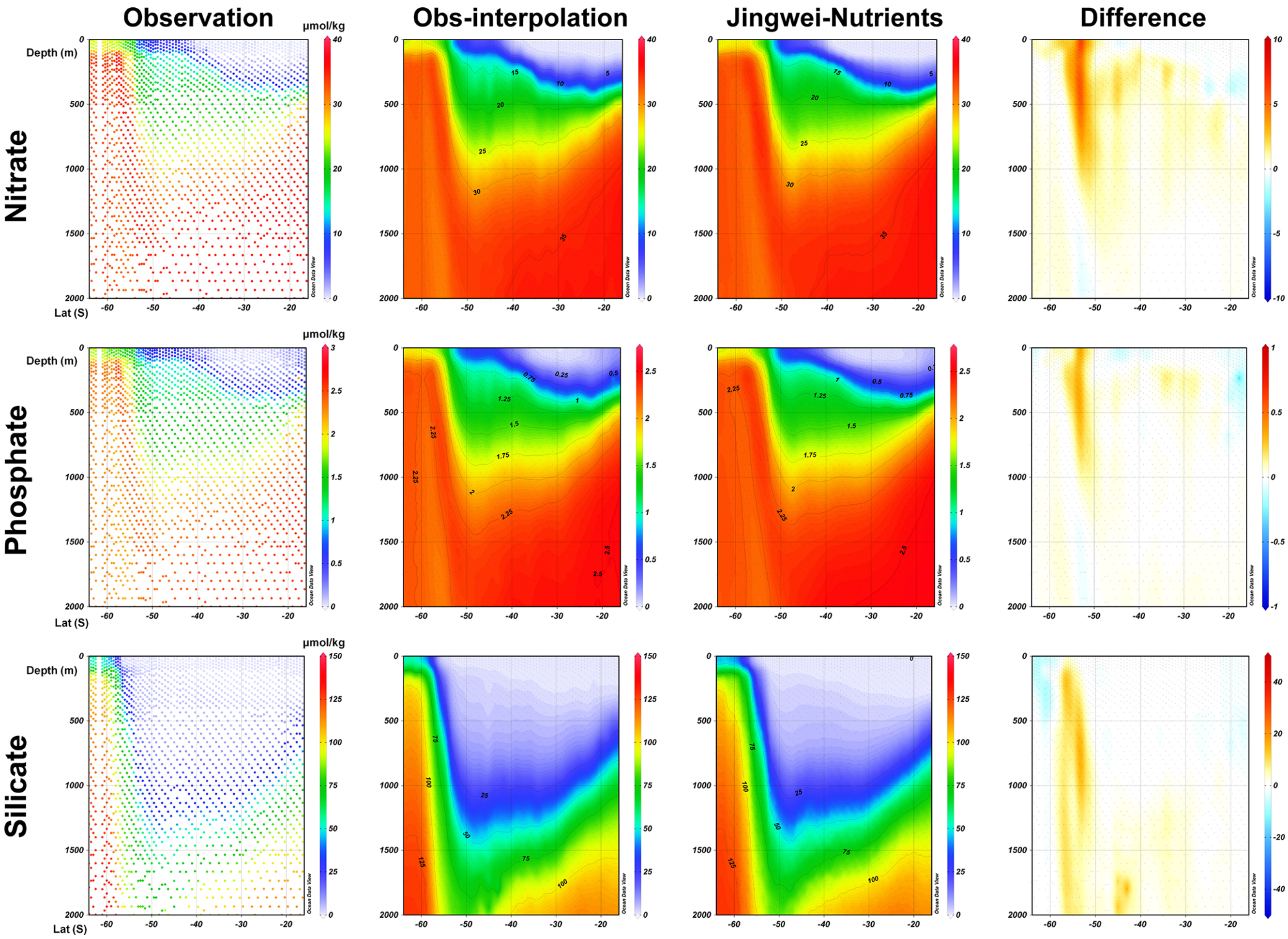

Figure 14. Spatial validation of nutrients along the P16S meridional section in the South Pacific and Southern Ocean. The panel layout and represented variables are identical to those in Fig. 13.

spread remains remarkably low relative to absolute concentrations – particularly across vast open-ocean basins – confirming the high stability and reliability of the product.

The top panels of Fig. 16 illustrate the depth-averaged spatial uncertainty for nitrate, phosphate, and silicate. The global maps reveal that the ensemble standard deviations are generally low across the open-ocean gyres, indicating model consensus in these environments. However, the uncertainty distribution exhibits spatial heterogeneities. For all three nutrients, higher uncertainties are localized along coastal margins and high-latitude boundary regions. Higher uncertainty values are observed in the subpolar North Pacific – specifically within the Bering Sea and the Sea of Okhotsk. These marginal seas are characterized by shelf-basin water exchanges, riverine inputs, and seasonal phytoplankton blooms, introducing greater natural variability. Furthermore, for silicate, a band of elevated uncertainty is observed across the Southern Ocean. This is consistent with the upwelling of the Antarctic Circumpolar Current and the presence of diatom blooms, which drive biogenic silica cycling (Tréguer et al., 2018), contributing to larger absolute variations compared to nitrate and phosphate.

The bottom panels of Fig. 16 track the temporal evolution of the global mean uncertainty from 1965 to 2023. The time-series demonstrates a long-term declining trend, corresponding to the historical evolution of global ocean observing systems. A notable decrease in the global mean Std occurs around 1990. This reduction in uncertainty aligns with the onset of the World Ocean Circulation Experiment (WOCE) (Siedler et al., 2001) and the Joint Global Ocean Flux Study (JGOFS) (Fasham, 2003), which marked the transition from sparse historical sampling to systematic global hydrographic surveys.

Entering the 21st century, the global mean uncertainties for all three nutrients remain generally stable at lower levels compared to earlier decades. For nitrate, the deployment of the Biogeochemical-Argo (BGC-Argo) float array post-2010 (Roemmich et al., 2019; Claustre et al., 2020) provided additional autonomous profiles, contributing to the sustained low uncertainty. For phosphate and silicate, despite the grad-

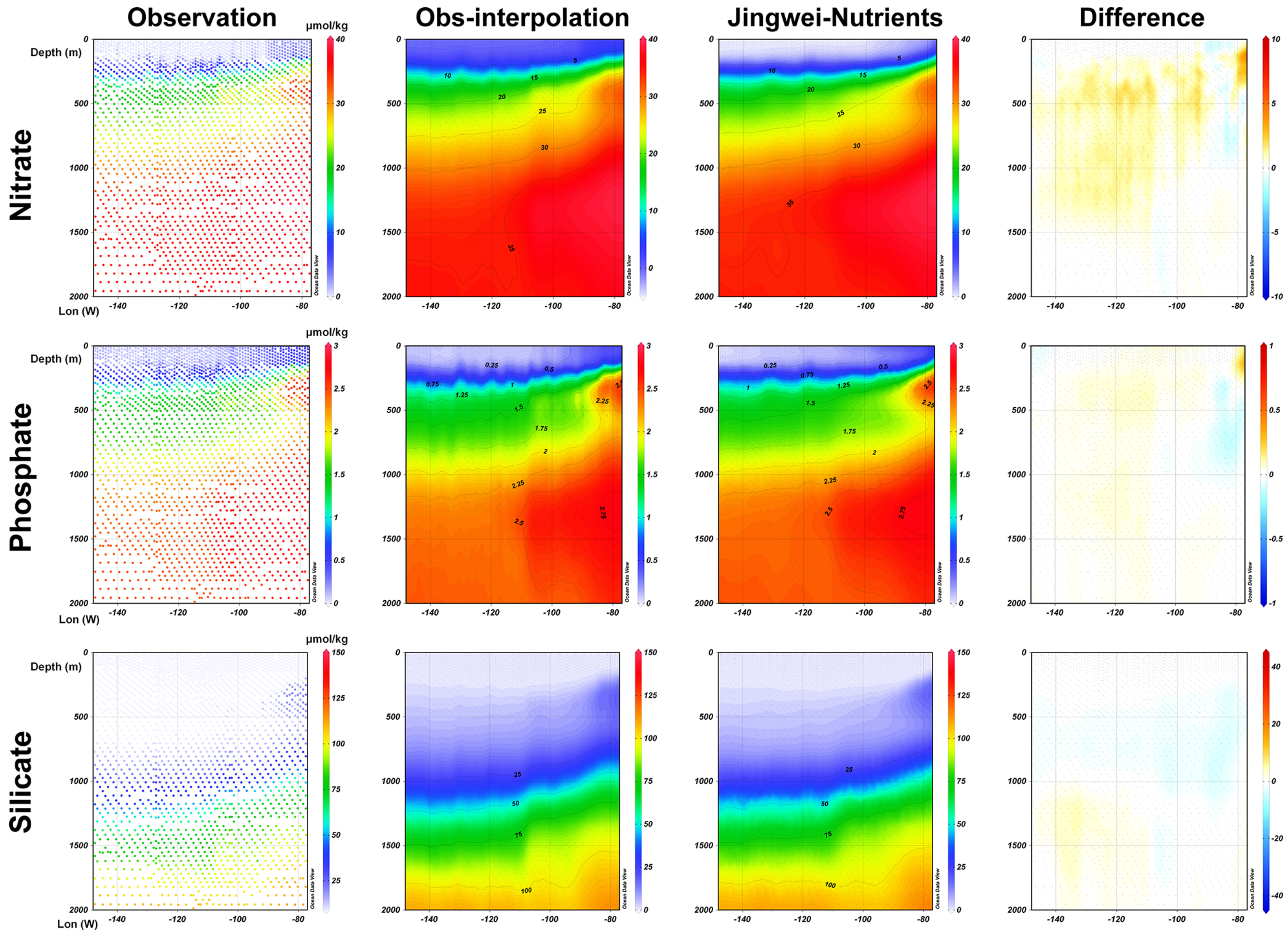

Figure 15. Spatial validation of nutrients along the P06E zonal section in the South Pacific. The panel layout and represented variables are identical to those in Fig. 13.

ual decline in traditional shipboard measurements in recent decades and the lack of Argo-based sensors for these elements, their mean uncertainties remain relatively low, though a slight upward trend is observable in the most recent years. Ultimately, this analysis indicates that the Jingwei-Nutrients product provides stable reconstructions, while also highlighting the regions and periods where data sparsity introduces greater variance.

4 Conclusion

In this study, we develop Jingwei-Nutrients, a global continuous data product of ocean nutrients (nitrate, phosphate, and silicate) at a monthly resolution, spanning from 1965 to 2023. This is achieved by employing a Multi-Task Learning (MTL) Transformer architecture, trained on quality-controlled historical observations from WOD, CCHDO, GLODAP, and the BGC-Argo float array. By extracting complex nonlinear relationships between discrete nutrient samples and continuous spatiotemporal hydrographic predictors, our approach effectively transforms sparse, unevenly distributed historical measurements into a continuous four-dimensional spatiotemporal field. This reconstruction expands the available nutrient data coverage, providing a global perspective on marine biogeochemical dynamics.

Validations across multiple scales support the reliability of the Jingwei-Nutrients product. The product accurately reproduces the climatological spatial distributions and phenological seasonal cycles of global nutrients, demonstrating consistency with the WOA23 climatology. The continuous reconstruction also captures the sharp physical-biogeochemical gradients and structural features inherent to the ocean interior. Independent synoptic validations using high-resolution GO-SHIP cruise sections (P16N, P16S, P06E) indicate the model's capacity to resolve complex three-dimensional features, including deep-basin nutrient accumulations, boundary upwelling, and dynamic mesoscale frontal zones. Furthermore, evaluations against long-term ecological time-series stations (HOT and KERFIX) show that the reconstruction captures localized interannual baselines and smooths short-

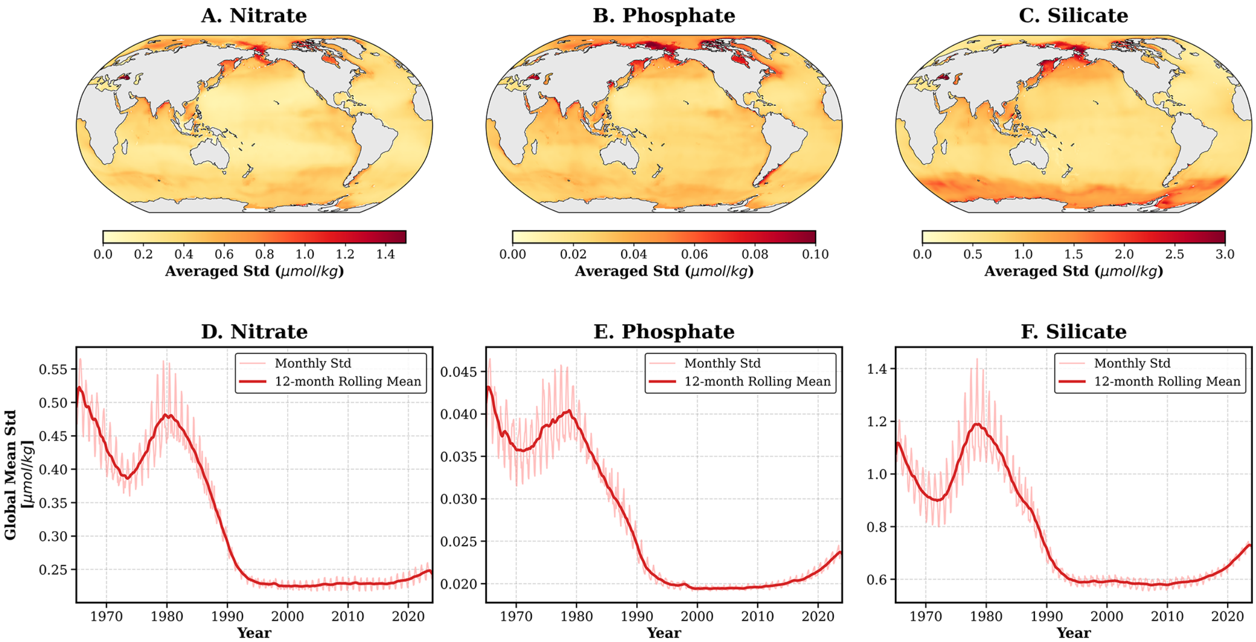

Figure 16. Spatiotemporal uncertainty analysis of the Jingwei-Nutrients reconstruction based on the ensemble standard deviation across the 6-fold cross-validation models. The top row displays the spatial distribution of the depth-averaged standard deviation for nitrate, phosphate, and silicate. The bottom row presents the temporal evolution of the global mean standard deviation from 1965 to 2023. Light red lines represent the raw monthly uncertainty, while the thick red lines indicate the 12-month rolling mean.

term variations while preserving primary physical and biological signals. Our spatiotemporal uncertainty analysis, derived from a 6-fold ensemble standard deviation, reveals a reduction in global reconstruction uncertainty following the WOCE/JGOFS era in the 1990s. Entering the 21st century, the uncertainty estimates continue to reflect the evolution of the global observing network.

Despite these advances, certain limitations remain in global-scale data-driven reconstructions. Regional uncertainties persist in dynamic marginal seas, coastal boundaries, and regions dominated by mesoscale eddies (e.g., the Subantarctic Front). Additionally, biological anomalies, such as the localized decoupling of the classical N:P uptake ratio driven by iron limitation in the Southern Ocean, pose challenges for generalized global models. Future efforts should focus on integrating higher-resolution sub-mesoscale physical forcings, assimilating emerging multi-sensor BGC-Argo data, and developing sub-regional modeling frameworks to better capture localized non-stationary biogeochemical processes.

The Jingwei-Nutrients data product provides a physically consistent baseline of global ocean nutrients over the past six decades. It offers an observational benchmark for evaluating Earth System Models (ESMs), supports investigations into long-term biogeochemical responses to anthropogenic climate change, and serves as high-resolution boundary conditions for future marine carbon cycle and ecosystem studies.

5 Data availability

The Jingwei-Nutrients data product presented in this article is openly available to the public. The reconstructed 4D global monthly fields spanning from 1965 to 2023 for nitrate, phosphate, and silicate can be accessed via Zenodo at https://doi.org/10.5281/zenodo.21066027 (Wang et al., 2026). The product is provided in standard NetCDF format.

The file contains monthly global reconstructed fields from January 1965 to December 2023. All nutrient variables are stored with dimensions (time, depth, lat, lon). The time dimension contains 708 monthly time steps, the depth dimension contains 67 standard levels from 0 to 2000 m, the latitude coordinate ranges from 82.5° S to 89.5° N, and the longitude coordinate ranges from 179.5° W to 179.5° E. The three main variables are nitrate, phosphate, and silicate, with units of $\mu mol\,kg^{-1}$. Missing or invalid ocean values are stored as NaN. The corresponding ensemble uncertainty files use the same coordinates, dimensions, depth levels, and missing-value convention as the main product. These files provide ensemble-based uncertainty estimates for nitrate, phosphate, and silicate, expressed as the standard deviation among ensemble members, with the same units as the reconstructed nutrient concentrations.

The primary in situ observation data used to train the data-driven non-linear models are harmonized from major public archives, including the World Ocean Database (WOD;

https://www.ncei.noaa.gov/products/world-ocean-database, last access: 16 July 2026, Boyer et al., 2018; Mishonov et al., 2024; Garcia et al., 2026), the Global Ocean Data Analysis Project (GLODAP; https://doi.org/10.25921/1f4w-0t92, Lauvset et al., 2022), the CLIVAR and Carbon Hydrographic Data Office (CCHDO; https://cchdo.ucsd.edu, last access: 16 July 2026, Sloyan et al., 2019), and the Argo program (https://doi.org/10.17882/42182, Argo, 2026; Claustre et al., 2020). The physical driver datasets and background reference fields, specifically the EN4 hydrographic objective analyses (https://www.metoffice.gov.uk/hadobs/en4/, last access: 16 July 2026, Good et al., 2013) and the World Ocean Atlas (WOA) climatologies (https://www.ncei.noaa.gov/products/world-ocean-atlas, last access: 16 July 2026, Locarnini et al., 2018, 2019; Zweng et al., 2018; Reagan et al., 2019; Garcia et al., 2024a, b), are publicly available from the Met Office Hadley Centre and the NOAA National Centers for Environmental Information (NCEI), respectively.

6 The Name of Jingwei

Jingwei is a classic figure in Chinese mythology, featured in the "Shan Hai Jing" (see https://en.wikipedia.org/wiki/Jingwei, last access: 16 July 2026). The story tells of Jingwei, the daughter of Emperor Yan, who drowned in the East Sea. She was reborn as a bird and decided to fill the sea with pebbles and twigs, endeavoring to prevent similar tragedies. Today, Jingwei symbolizes perseverance and determination, embodying the spirit of never giving up despite difficult challenges.

This project is named Jingwei-Nutrients to honor the collective determination of generations of oceanographers, researchers, and vessel crews. The historical biogeochemical observations they have painstakingly collected – often scattered across vast spatial scales and decades of time – might appear as fragmented as the pebbles carried by Jingwei. Yet, it is through the persistent accumulation of these "pebbles" of data that we can finally reconstruct the complex patterns of global nutrient cycling. This name serves as a tribute to those who venture into the field to sense the pulse of our oceans, embodying the spirit of persistent exploration that makes global-scale synthesis possible.

Author contributions. BL, MJ, and ZW designed the study and product. ZW and YX collected and processed the data, developed the code, and performed the analysis. TI, LZ, LC, YL, and XW provided methodological guidance and advice. ZW wrote the original draft. All authors reviewed and edited the manuscript.

Competing interests. The contact author has declared that none of the authors has any competing interests.

Acknowledgements. We extend our sincere gratitude to Jonathan D. Sharp (University of Washington CICOES/PMEL) for his valuable suggestions and insightful discussions regarding the nutrient reconstruction work. We thank the CCHDO, the WOD, GLODAP, and the BGC-Argo program for providing the observational data used in this study. Special thanks are owed to all scientists and vessel crews involved in data collection, analysis, and management for these programs.

Financial support. This study is funded by the National Natural Science Foundation of China (grants T2421002, 62602003, and 62272293), the Postdoctoral Fellowship Program of CPSF (grant GZB20250806), and the AI for Science Seed Program of Shanghai Jiao Tong University (grant 2025AI4S-QY01).

Review statement. This paper was edited by Frédéric Gazeau and reviewed by two anonymous referees.

References

Argo: Argo float data and metadata from Global Data Assembly Centre (Argo GDAC), SEANOE [data set] https://doi.org/10.17882/42182, 2026.

Ascani, F., Richards, K. J., Firing, E., Grant, S., Johnson, K. S., Jia, Y., Lukas, R., and Bidigare, R. R.: Physical and biological controls of nitrate concentrations in the upper subtropical North Pacific Ocean, Deep-Sea Res. Pt. II, 93, 119–134, https://doi.org/10.1016/j.dsr2.2013.01.034, 2013.

Behrenfeld, M. J., O'Malley, R. T., Siegel, D. A., McClain, C. R., Sarmiento, J. L., Feldman, G. C., Milligan, A. J., Falkowski, P. G., Letelier, R. M., and Boss, E. S.: Climate-driven trends in contemporary ocean productivity, Nature, 444, 752–755, https://doi.org/10.1038/nature05317, 2006.

Benitez-Nelson, C. R., Bidigare, R. R., Dickey, T. D., Landry, M. R., Leonard, C. L., Brown, S. L., Nencioli, F., Rii, Y. M., Maiti, K., Becker, J. W., Bibby, T. S., Black, W., Cai, W.-J., Carlson, C. A., Chen, F., Kuwahara, V. S., Mahaffey, C., McAndrew, P. M., Quay, P. D., Rappé, M. S., Selph, K. E., Simmons, M. P., and Yang, E. J.: Mesoscale Eddies Drive Increased Silica Export in the Subtropical Pacific Ocean, Science, 316, 1017–1021, https://doi.org/10.1126/science.1136221, 2007.

Bi, K., Xie, L., Zhang, H., Chen, X., Gu, X., and Tian, Q.: Accurate medium-range global weather forecasting with 3D neural networks, Nature, 619, 533–538, https://doi.org/10.1038/s41586-023-06185-3, 2023.

Bittig, H. C., Steinhoff, T., Claustre, H., Fiedler, B., Williams, N. L., Sauzède, R., Körtzinger, A., and Gattuso, J.-P.: An alternative to static climatologies: Robust estimation of open ocean CO_2 variables and nutrient concentrations from T, S, and O_2 data using Bayesian neural networks, Front. Mar. Sci., 5, 328, https://doi.org/10.3389/fmars.2018.00328, 2018.

Boyd, P. W., Jickells, T., Law, C. S., Blain, S., Boyle, E. A., Buesseler, K. O., Coale, K. H., Cullen, J. J., de Baar, H. J. W., Follows, M., Harvey, M., Lancelot, C., Levasseur, M., Owens, N. P. J., Pollard, R., Rivkin, R. B., Sarmiento, J., Schoemann, V., Smetacek, V., Takeda, S., Tsuda, A., Turner, S., and Watson, A. J.: Mesoscale iron enrichment experiments 1993–2005: Synthesis and future directions, Science, 315, 612–617, https://doi.org/10.1126/science.1131669, 2007.

Boyer, T. P., Baranova, O. K., Coleman, C., Garcia, H. E., Grodsky, A., Locarnini, R. A., Mishonov, A. V., Paver, C. R., Reagan, J. R., Seidov, D., Smolyar, I. V., Weathers, K. W., and Zweng, M. M.: World Ocean Database 2018, A. V. Mishonov, Technical Editor, NOAA Atlas NESDIS 87, 2018.

Broecker, W. S.: The great ocean conveyor, Oceanography, 4, 79–89, https://doi.org/10.5670/oceanog.1991.07, 1991.

Broullón, D., Pérez, F. F., Velo, A., Hoppema, M., Olsen, A., Takahashi, T., Key, R. M., Tanhua, T., González-Dávila, M., Jeansson, E., Kozyr, A., and van Heuven, S. M. A. C.: A global monthly climatology of total alkalinity: a neural network approach, Earth Syst. Sci. Data, 11, 1109–1127, https://doi.org/10.5194/essd-11-1109-2019, 2019.

Browning, T. J. and Moore, C. M.: Global analysis of ocean phytoplankton nutrient limitation reveals high prevalence of co-limitation, Nat. Commun., 14, 5014, https://doi.org/10.1038/s41467-023-40774-0, 2023.

Carter, B. R., Bittig, H. C., Fassbender, A. J., Sharp, J. D., Takeshita, Y., Xu, Y.-Y., Álvarez, M., Wanninkhof, R., Feely, R. A., and Barbero, L.: New and updated global empirical seawater property estimation routines, Limnol. Oceanogr. Meth., 19, 785–809, https://doi.org/10.1002/lom3.10461, 2021.

Chavez, F. P. and Messié, M.: A comparison of eastern boundary upwelling ecosystems, Prog. Oceanogr., 83, 80–96, https://doi.org/10.1016/j.pocean.2009.07.032, 2009.

Cheng, L., Trenberth, K. E., Fasullo, J., Boyer, T., Abraham, J., and Zhu, J.: Improved estimates of ocean heat content from 1960 to 2015, Sci. Adv., 3, e1601545, https://doi.org/10.1126/sciadv.1601545, 2017.

Claustre, H., Johnson, K. S., and Takeshita, Y.: Observing the global ocean with biogeochemical-Argo, Annu. Rev. Mar. Sci., 12, 23–48, https://doi.org/10.1146/annurev-marine-010419-010956, 2020.

Deutsch, C. and Weber, T.: Nutrient Ratios as a Tracer and Driver of Ocean Biogeochemistry, Annu. Rev. Mar. Sci., 4, 113–141, https://doi.org/10.1146/annurev-marine-120709-142821, 2012.

Du, C., Zheng, N., Kao, S.-J., Dai, M., Cao, Z., Shi, D., Li, Q., Wang, H., Luo, X., and Li, X.: A historical nutrient dataset (1895–2024) for the North Pacific: reconstructed from machine learning and hydrographic observations, Earth Syst. Sci. Data, 18, 2951–2969, https://doi.org/10.5194/essd-18-2951-2026, 2026.

Fasham, M. J. R. (Ed.): Ocean Biogeochemistry: The Role of the Ocean Carbon Cycle in Global Change, Springer, Berlin, Heidelberg, https://doi.org/10.1007/978-3-642-55844-3, 2003.

Garcia, H. E., Weathers, K. W., Paver, C. R., Smolyar, I. V., Boyer, T. P., Locarnini, R. A., Zweng, M. M., Mishonov, A. V., Baranova, O. K., Seidov, D., and Reagan, J. R.: World Ocean Atlas 2018, Volume 4: Dissolved Inorganic Nutrients (phosphate, nitrate and nitrate+nitrite, silicate), A. Mishonov Technical Ed., NOAA Atlas NESDIS 84, 35 pp., https://doi.org/10.25923/ng6j-ey81, 2018.

Garcia, H. E., Bouchard, C., Cross, S. L., Paver, C. R., Wang, Z., Reagan, J. R., Boyer, T. P., Locarnini, R. A., Mishonov, A. V., Baranova, O. K., Seidov, D., and Dukhovskoy, D.: World Ocean Atlas 2023, Volume 4: Dissolved Inorganic Nutrients (phosphate, nitrate, and silicate), A. Mishonov, Tech. Ed., NOAA Atlas NESDIS 92, https://doi.org/10.25923/39qw-7j08, 2024a.

Garcia, H. E., Wang, Z., Bouchard, C., Cross, S. L., Paver, C. R., Reagan, J. R., Boyer, T. P., Locarnini, R. A., Mishonov, A. V., Baranova, O. K., Seidov, D., and Dukhovskoy, D.: World Ocean Atlas 2023, Volume 3: Dissolved Oxygen, Apparent Oxygen Utilization, and Oxygen Saturation, A. Mishonov, Tech. Ed., NOAA Atlas NESDIS 91, https://doi.org/10.25923/rb67-ns53, 2024b.

Garcia, H. E., Boyer, T. P., Levitus, S., Reagan, J. R., Mishonov, A. V., Jiang, L.-Q., Wang, Z., Paver, C. R., Nyadjro, E., Cross, S., Bouchard, C., Hogan, P., Baranova, O. K., and Locarnini, R. A.: World Ocean Database 2023: A foundational data resource for and by the global ocean and coastal communities, Sci. Data, 13, 613, https://doi.org/10.1038/s41597-026-06957-2, 2026.

Good, S. A., Martin, M. J., and Rayner, N. A.: EN4: Quality controlled ocean temperature and salinity profiles and monthly objective analyses with uncertainty estimates, J. Geophys. Res.-Oceans, 118, 6704–6716, https://doi.org/10.1002/2013JC009067, 2013.

Gouretski, V. and Reseghetti, F.: On depth and temperature biases in bathythermograph data: Development of a new correction scheme based on analysis of a global ocean database, Deep-Sea Res. Pt. I, 57, 812–833, https://doi.org/10.1016/j.dsr.2010.03.011, 2010.

Gregor, L., Lebehot, A. D., Kok, S., and Scheel Monteiro, P. M.: A comparative assessment of the uncertainties of global surface ocean CO_2 estimates using a machine-learning ensemble (CSIR-ML6 version 2019a) – have we hit the wall?, Geosci. Model Dev., 12, 5113–5136, https://doi.org/10.5194/gmd-12-5113-2019, 2019.

Ito, T., Minobe, S., Long, M. C., and Deutsch, C.: Upper ocean O_2 trends: 1958–2015, Geophys. Res. Lett., 44, 4214–4223, https://doi.org/10.1002/2017GL073613, 2017.

Ito, T., Cervania, A., Cross, K., Ainchwar, S., and Delawalla, S.: Mapping dissolved oxygen concentrations by combining shipboard and Argo observations using machine learning algorithms, J. Geophys. Res.-Mach. Learn. Comput., 1, e2024JH000272, https://doi.org/10.1029/2024JH000272, 2024.

Ito, T., Garcia, H. E., Wang, Z., Cheng, L., Du, J., Roach, C. J., Zhou, Y., Sharp, J. D., Lauvset, S. K., Minobe, S., Bushinsky, S., Lu, B., and Navarra, G.: Assessing the observational uncertainties of dissolved oxygen climatology and seasonal cycle through a coordinated intercomparison project, Global Biogeochem. Cy., 39, e2025GB008751, https://doi.org/10.1029/2025GB008751, 2025.

Jeandel, C., Ruiz-Pino, D., Gasser, B., Etcheber, H., Brunet, C., Poisson, A., and Cronis, S.: KERFIX, a time-series station in the Southern Ocean: a presentation, J. Marine Syst., 17, 555–569, https://doi.org/10.1016/S0924-7963(98)00064-5, 1998.

Karl, D. M. and Lukas, R.: The Hawaii Ocean Time-series (HOT) program: Background, rationale and implementation, Deep-Sea Res. Pt. II, 43, 129–156, https://doi.org/10.1016/0967-0645(96)00005-7, 1996.

Kendall, A., Gal, Y., and Cipolla, R.: Multi-Task Learning Using Uncertainty to Weigh Losses for Scene Geometry and Semantics, in: Proceedings of the IEEE Conference on Computer Vision and Pattern Recognition (CVPR), 7482–7491, https://doi.org/10.1109/CVPR.2018.00781, 2018.

Keppler, L., Landschützer, P., Gruber, N., Lauvset, S. K., and Stemmler, I.: Seasonal carbon dynamics in the near-global ocean, Global Biogeochem. Cy., 34, e2020GB006571, https://doi.org/10.1029/2020GB006571, 2020.

Lam, R., Sanchez-Gonzalez, A., Willson, M., Wirnsberger, P., Fortunato, M., Alet, F., Ravuri, S., Ewalds, T., Eaton-Rosen, Z., Hu, W., Merose, A., Hoyer, S., Holland, G., Vinyals, O., Stott, J., Pritzel, A., Mohamed, S., and Battaglia, P.: Learning skillful medium-range global weather forecasting, Science, 382, 1416–1421, https://doi.org/10.1126/science.adi2336, 2023.

Landschützer, P., Gruber, N., and Bakker, D. C. E.: Decadal variations and trends of the global ocean carbon sink, Global Biogeochem. Cy., 30, 1396–1417, https://doi.org/10.1002/2015GB005359, 2016.

Lauvset, S. K., Lange, N., Tanhua, T., Bittig, H. C., Olsen, A., Kozyr, A., Alin, S., Álvarez, M., Azetsu-Scott, K., Barbero, L., Becker, S., Brown, P. J., Carter, B. R., da Cunha, L. C., Feely, R. A., Hoppema, M., Humphreys, M. P., Ishii, M., Jeansson, E., Jiang, L.-Q., Jones, S. D., Lo Monaco, C., Murata, A., Müller, J. D., Pérez, F. F., Pfeil, B., Schirnick, C., Steinfeldt, R., Suzuki, T., Tilbrook, B., Ulfsbo, A., Velo, A., Woosley, R. J., and Key, R. M.: GLODAPv2.2022: the latest version of the global interior ocean biogeochemical data product, Earth Syst. Sci. Data, 14, 5543–5572, https://doi.org/10.5194/essd-14-5543-2022, 2022.

Levitus, S.: Climatological Atlas of the World Ocean, NOAA Professional Paper 13, US Government Printing Office, Washington, D.C., 173 pp., 1982.

Liu, J., Wang, H., Mou, J., Peñuelas, J., Delgado-Baquerizo, M., Martiny, A. C., Zhou, G., Hutchins, D. A., Inomura, K., Lomas, M. W., Fakhraee, M., Pellegrini, A., Kohler, T. J., Deutsch, C. A., Planavsky, N., Lapointe, B., Zhang, Y., Li, Y., Zhou, J., Zhang, Y., Sun, S., Li, Y., Zhang, W., Cao, J., and Chen, J.: Global-scale shifts in marine ecological stoichiometry over the past 50 years, Nat. Geosci., 18, 769–778, https://doi.org/10.1038/s41561-025-01735-y, 2025.

Locarnini, R. A., Mishonov, A. V., Baranova, O. K., Boyer, T. P., Zweng, M. M., Garcia, H. E., Reagan, J. R., Seidov, D., Weathers, K. W., Paver, C. R., and Smolyar, I. V.: World Ocean Atlas 2018, Volume 1: Temperature, A. Mishonov Technical Ed., NOAA Atlas NESDIS 81, 52 pp., https://doi.org/10.25923/e5rn-9711, 2018.

Locarnini, R. A., Boyer, T. P., Mishonov, A. V., Reagan, J. R., Zweng, M. M., Baranova, O. K., Garcia, H. E., Seidov, D., Weathers, K. W., Paver, C. R., and Smolyar, I. V.: World Ocean Atlas 2018, Volume 5: Density, A. Mishonov, Technical Editor, NOAA Atlas NESDIS 85, 41 pp., https://doi.org/10.25923/xnf9-9s53, 2019.

Longhurst, A. R.: Ecological Geography of the Sea, 2nd Edn., Academic Press, Burlington, MA, 560 pp., https://doi.org/10.1016/B978-0-12-455521-1.X5000-1, 2007.

Lu, B., Zhao, Z., Han, L., Gan, X., Zhou, Y., Zhou, L., Fu, L., Wang, X., Zhou, C., and Zhang, J.: OxyGenerator: Reconstructing global ocean deoxygenation over a century with deep learning, in: Proceedings of the 41st International Conference on Machine Learning, Proceedings of Machine Learning Research, 235, 33219–33242, 2024.

Marshall, J. and Speer, K.: Closure of the meridional overturning circulation through Southern Ocean upwelling, Nat. Geosci., 5, 171–180, https://doi.org/10.1038/ngeo1391, 2012.

Mishonov, A. V., Boyer, T. P., Baranova, O. K., Bouchard, C. N., Cross, S., Garcia, H. E., Locarnini, R. A., Paver, C. R., Reagan, J. R., Wang, Z., Seidov, D., Grodsky, A. I., and Beauchamp, J. G.: World Ocean Database 2023, NOAA Atlas NESDIS 97, 206 pp., https://doi.org/10.25923/z885-h264, 2024.

Moore, C. M., Mills, M. M., Arrigo, K. R., Berman-Frank, I., Bopp, L., Boyd, P. W., Galbraith, E. D., Geider, R. J., Guieu, C., Jaccard, S. L., Jickells, T. D., Lenton, T. M., Mahowald, N. M., Marañón, E., Marinov, I., Moore, J. K., Nakatsuka, T., Oschlies, A., Saito, M. A., Thingstad, T., Tsuda, A., and Ulloa, O.: Processes and patterns of oceanic nutrient limitation, Nat. Geosci., 6, 701–710, https://doi.org/10.1038/ngeo1765, 2013.

Olsen, A., Key, R. M., van Heuven, S., Lauvset, S. K., Velo, A., Lin, X., Schirnick, C., Kozyr, A., Tanhua, T., Hoppema, M., Jutterström, S., Steinfeldt, R., Jeansson, E., Ishii, M., Pérez, F. F., and Suzuki, T.: The Global Ocean Data Analysis Project version 2 (GLODAPv2) – an internally consistent data product for the world ocean, Earth Syst. Sci. Data, 8, 297–323, https://doi.org/10.5194/essd-8-297-2016, 2016.

Paulmier, A. and Ruiz-Pino, D.: Oxygen minimum zones (OMZs) in the modern ocean, Prog. Oceanogr., 80, 113–128, https://doi.org/10.1016/j.pocean.2008.08.001, 2009.

Reagan, J. R., Zweng, M. M., Seidov, D., Boyer, T. P., Locarnini, R. A., Mishonov, A. V., Baranova, O. K., Garcia, H. E., Weathers, K. W., Paver, C. R., Smolyar, I. V., and Tyler, R. H.: World Ocean Atlas 2018, Volume 6: Conductivity, NOAA Atlas NESDIS 86, 38 pp., https://doi.org/10.25923/wjeq-s877, 2019.

Redfield, A. C.: On the proportions of organic derivatives in sea water and their relation to the composition of plankton, in: James Johnstone Memorial Volume, edited by: Daniel, R. J., University Press of Liverpool, Liverpool, 176–192, 1934.

Reichstein, M., Camps-Valls, G., Stevens, B., Jung, M., Denzler, J., Carvalhais, N., and Prabhat: Deep learning and process understanding for data-driven Earth system science, Nature, 566, 195–204, https://doi.org/10.1038/s41586-019-0912-1, 2019.

Roemmich, D., Alford, M. H., Claustre, H., Johnson, K., King, B., Moum, J., Oke, P., Owens, W. B., Pouliquen, S., Purkey, S., Scanderbeg, M., Suga, T., Wijffels, S., Zilberman, N., Bakker, D., Baringer, M., Belbeoch, M., Bittig, H. C., Boss, E., Calil, P., Carse, F., Carval, T., Chai, F., Conchubhair, D. Ó., d'Ortenzio, F., Dall'Olmo, G., Desbruyeres, D., Fennel, K., Fer, I., Ferrari, R., Forget, G., Freeland, H., Fujiki, T., Gehlen, M., Greenan, B., Hallberg, R., Hibiya, T., Hosoda, S., Jayne, S., Jochum, M., Johnson, G. C., Kang, K., Kolodziejczyk, N., Körtzinger, A., Le Traon, P.-Y., Lenn, Y.-D., Maze, G., Mork, K. A., Morris, T., Nagai, T., Nash, J., Naveira Garabato, A., Olsen, A., Pattabhi, R. R., Prakash, S., Riser, S., Schmechtig, C., Schmid, C., Shroyer, E., Sterl, A., Sutton, P., Talley, L., Tanhua, T., Thierry, V., Thomalla, S., Toole, J., Troisi, A., Trull, T. W., Turton, J., Velez-Belchi, P. J., Walczowski, W., Wang, H., Wanninkhof, R., Waterhouse, A. F., Waterman, S., Watson, A., Wilson, C., Wong, A. P. S., Xu, J., and Yasuda, I.: On the Future of Argo: A Global, Full-Depth, Multi-Disciplinary Array, Front. Mar. Sci., 6, 439, https://doi.org/10.3389/fmars.2019.00439, 2019.

Sarmiento, J. L. and Gruber, N.: Ocean Biogeochemical Dynamics, Princeton University Press, Princeton, NJ, 526 pp., https://doi.org/10.1515/9781400849079, 2006.

Sauzède, R., Bittig, H. C., Claustre, H., Pasqueron de Fommervault, O., Gattuso, J.-P., Legendre, L., and Johnson, K. S.: Estimates of water-column nutrient concentrations and carbonate system parameters in the global ocean: A novel approach based on neural networks, Front. Mar. Sci., 4, 128, https://doi.org/10.3389/fmars.2017.00128, 2017.

Siedler, G., Church, J., and Gould, J. (Eds.): Ocean Circulation and Climate: Observing and Modelling the Global Ocean, Academic Press, San Diego, CA, 716 pp., https://doi.org/10.1016/S0074-6142(01)X8034-0, 2001.

Sigman, D. M. and Hain, M. P.: The Biological Productivity of the Ocean, Nat. Educ. Knowl., 3, 21, https://www.nature.com/scitable/knowledge/library/the-biological-productivity-of-the-ocean-70631104/ (last access: 16 July 2026), 2012.

Sloyan, B. M., Wanninkhof, R., Kramp, M., Johnson, G. C., Talley, L. D., Tanhua, T., McDonagh, E., Cusack, C., O'Rourke, E., McGovern, E., Katsumata, K., Diggs, S., Hummon, J., Ishii, M., Azetsu-Scott, K., Boss, E., Ansorge, I., Perez, F. F., Mercier, H., Williams, M. J. M., Anderson, L., Lee, J. H., Murata, A., Kouketsu, S., Jeansson, E., Hoppema, M., and Campos, E.: The Global Ocean Ship-Based Hydrographic Investigations Program (GO-SHIP): A Platform for Integrated Multidisciplinary Ocean Science, Front. Mar. Sci., 6, 445, https://doi.org/10.3389/fmars.2019.00445, 2019.

Sonnewald, M., Lguensat, R., Jones, D. C., Dueben, P. D., Brajard, J., and Balaji, V.: Bridging observations, theory and numerical simulation of the ocean using machine learning, Environ. Res. Lett., 16, 073008, https://doi.org/10.1088/1748-9326/ac0eb0, 2021.

Sundararaman, H. K. K. and Shanmugam, P.: Estimates of the global ocean surface dissolved oxygen and macronutrients from satellite data, Remote Sens. Environ., 311, 114243, https://doi.org/10.1016/j.rse.2024.114243, 2024.

Talley, L. D.: Closure of the global overturning circulation through the Indian, Pacific, and Southern Oceans: Schematics and transports, Oceanography, 26, 80–97, https://doi.org/10.5670/oceanog.2013.07, 2013.

Tréguer, P., Bowler, C., Moriceau, B., Dutkiewicz, S., Gehlen, M., Aumont, O., Bittner, L., Dugdale, R., Finkel, Z., Iudicone, D., Jahn, O., Guidi, L., Lasbleiz, M., Leblanc, K., Levy, M., and Pondaven, P.: Influence of diatom diversity on the ocean biological carbon pump, Nat. Geosci., 11, 27–37, https://doi.org/10.1038/s41561-017-0028-x, 2018.

Vandenhende, S., Georgoulis, S., Van Gansbeke, W., Proesmans, M., Dai, D., and Van Gool, L.: Multi-task learning for dense prediction tasks: A survey, IEEE Trans. Pattern Anal. Mach. Intell., 44, 3614–3633, https://doi.org/10.1109/TPAMI.2021.3054719, 2022.

Vaswani, A., Shazeer, N., Parmar, N., Uszkoreit, J., Jones, L., Gomez, A. N., Kaiser, Ł., and Polosukhin, I.: Attention Is All You Need, Adv. Neur. In., 30, 5998–6008, https://doi.org/10.48550/arXiv.1706.03762, 2017.

Wang, Z., Lu, B., Xin, Y., Ito, T., Zhou, L., Cheng, L., Li, Y., Wang, X., Zhou, C., and Jin, M.: Jingwei-Nutrients: A global spatiotemporal reconstruction of ocean nutrients (1965–2023) using multi-task deep learning, Zenodo [data set], https://doi.org/10.5281/zenodo.21066027, 2026.

Yu, T., Kumar, S., Gupta, A., Levine, S., Hausman, K., and Finn, C.: Gradient Surgery for Multi-Task Learning, Adv. Neur. In., 33, 5824–5836, https://doi.org/10.48550/arXiv.2001.06782, 2020.

Yu, X., Guo, H., Zhang, J., Ma, Y., Wang, X., Liu, G., Xing, M., Xu, N., and Seka, A. M.: A continual-learning-based multilayer perceptron for improved reconstruction of three-dimensional nitrate concentrations, Earth Syst. Sci. Data, 17, 2735–2759, https://doi.org/10.5194/essd-17-2735-2025, 2025.

Zanna, L., Khatiwala, S., Gregory, J. M., Ison, J., and Heimbach, P.: Global reconstruction of historical ocean heat storage and transport, P. Natl. Acad. Sci. USA, 116, 1126–1131, https://doi.org/10.1073/pnas.1808838115, 2019.

Zweng, M. M., Reagan, J. R., Seidov, D., Boyer, T. P., Locarnini, R. A., Garcia, H. E., Mishonov, A. V., Baranova, O. K., Weathers, K. W., Paver, C. R., and Smolyar, I. V.: World Ocean Atlas 2018, Volume 2: Salinity, A. Mishonov, Technical Ed., NOAA Atlas NESDIS 82, 50 pp., https://doi.org/10.25923/9pgv-1224, 2018.